Main Manuscript for

An engineered multifunctional protein tag for advanced fluorescence imaging

Hela Benaissa[1,2], Karim Ounoughi[2], Isabelle Aujard[2], Evelyne Fischer[3], Rosette Goïame[3], Julie Nguyen[4], Alison G. Tebo[1,2,#], Chenge Li[2,##], Thomas Le Saux[2], Lydia Danglot[4,5], Nicolas Pietrancosta[1,6], Xavier Morin[3], Ludovic Jullien[2] & Arnaud Gautier[1,2,7,*]

[1] Sorbonne Université, École Normale Supérieure, Université PSL, CNRS, Laboratoire des Biomolécules, LBM, 75005 Paris, France
[2] PASTEUR, Department of Chemistry, École Normale Supérieure, Université PSL, Sorbonne Université, CNRS, 75005 Paris, France
[3] Institut de Biologie de l'ENS (IBENS), École Normale Supérieure, CNRS, INSERM, Université PSL, 75005 Paris, France
[4] Université de Paris, NeurImag Imaging Facility, Institute of Psychiatry and Neuroscience of Paris, INSERM U1266, 75014 Paris, France.
[5] Université de Paris, Institute of Psychiatry and Neuroscience of Paris, INSERM U1266, Membrane Traffic in Healthy & Diseased Brain, 75014 Paris, France.
[6] Neuroscience Paris Seine-Institut de Biologie Paris Seine (NPS-IBPS) INSERM, CNRS, Sorbonne Université, Paris, France
[7] Institut Universitaire de France
[#] Current address: Janelia Research Campus, Howard Hughes Medical Institute, Ashburn, VA 20147, USA
[##] Current address: (a) Department of Obstetrics and Gynecology, Ren Ji Hospital, School of Medicine, Shanghai Jiao Tong University; (b) State Key Laboratory of Oncogenes and Related Genes, Shanghai Cancer Institute, Ren Ji Hospital, School of Medicine, Shanghai Jiao Tong University

*Arnaud Gautier.

Email: arnaud.gautier@sorbonne-universite.fr

Author Contributions: H.B., I.A., L.D., N.P., X.M., L.J. and A.G. designed the experiments. H.B., K.O., E.F., R.G., J.N., I.A., T.L.S., A.G.T., C.L., L.D., N.P., X.M. and A.G. performed the experiments. H.B., E.F., L.D., N.P., X.M., L.J. and A.G. analyzed the experiments. H.B. and A.G. wrote the paper with the help of all the authors.

Competing Interest Statement: The authors declare the following competing financial interest: A.G. and L.J. are cofounders and hold equity in Twinkle Bioscience/The Twinkle Factory, a company commercializing the FAST technology.

Keywords: chemogenetic fluorescent reporters ; directed evolution ; fluorescence imaging ; live cell imaging ; super-resolution microscopy.

This PDF file includes: Main Text & Figures 1 to 6

Abstract

Fluorescent reporters are essential tools in cell biology for imaging the dynamics of proteins in living cells and organisms with high spatial and temporal resolution. Chemogenetic systems made of a genetically encoded protein tag acting as an anchor for synthetic fluorophores combine the targeting selectivity of genetic tags with the advantages of synthetic fluorophores. Here, we present the directed evolution of a small 14-kDa protein tag with extended chromophore promiscuity capable of efficiently forming non-covalent fluorescent assemblies with a collection of membrane-permeant and membrane-impermeant fluorogenic chromophores displaying spectral properties spanning the entire visible spectrum. The ability to adapt the fluorescence color by choosing a different live-cell compatible fluorogenic chromophore enables to genetically encode blue, cyan, green, yellow, orange and red fluorescence with a single tag, providing an unprecedent experimental versatility. The possibility to form dark assemblies using non-fluorescent chromophores provides moreover an innovative way for switching off fluorescence on-demand in cells and organisms with high temporal resolution by chromophore replacement. Selective wash-free fluorogenic labeling of fusion proteins could be achieved with high efficiency in live cells, including delicate cultured hippocampal neurons, and in multicellular organisms, allowing high contrast imaging with various advanced microscopy techniques. The remarkable labeling efficiency and fluorescence performance allowed the multicolor imaging of dynamic processes in multicellular systems. The ability to match the spectral properties to the imaging modalities and the high photostability enabled to achieve efficient stimulated emission depletion (STED) nanoscopy of fusion proteins in live cells and live primary cultured neurons.

Introduction

Our understanding of cells and organisms is intricately related to our ability to observe how their constituents organize and interact. Optical microscopy techniques have become essential in biology as they enable one to study the dynamics of fluorescently labeled structures and biomolecules with unprecedented sensitivity and spatiotemporal resolution. The discovery and development of the green fluorescent protein (GFP) and its analogs enabled the selective labeling of virtually any protein through simple genetic fusion (1). Although fluorescent proteins provide one of the most powerful techniques for imaging proteins in live cells, they have specific limitations that prevent their unrestricted use in molecular imaging. Their size and tendency to oligomerize can lead to dysfunctional fusions, their long fluorescence maturation time can prevent the study of dynamic processes, and their need for molecular oxygen prevents imaging under anaerobic processes (2).These challenges have motivated the development of new reporters made of a genetic tag that act as an anchor for the selective binding of synthetic fluorescent probes (3) (4) (5) (6) (7). These chemogenetic reporters combine the targeting selectivity of genetic tags with the advantages of synthetic organic fluorophores, which can exhibit higher brightness and photostability (8) (9), and be tuned at will by molecular engineering (10). Their modular nature opens moreover new prospects for innovative on-demand bioimaging and biosensing (11) (12) (13).

To achieve labeling specificity comparable to fluorescent proteins while circumventing some of their limitations, we have recently developed a small monomeric protein, named FAST (Fluorescence-Activating and absorption-Shifting Tag), able to form with exquisite specificity non-covalent fluorescent assemblies with substituted 4-hydroxybenzylidene rhodanine (HBR) derivatives (14). Because HBR analogs exhibit otherwise essentially undetectable fluorescence in solution or in cells, selective imaging of FAST-tagged proteins can be achieved without the need for washing the free ligand in excess, facilitating the study of dynamic processes and the imaging of multicellular organisms. FAST has several advantages over fluorescent proteins: it is a small tag of 14 kDa (125 amino acid residues) with a reduced genetic footprint, which fluoresces instantaneously, functions in absence of molecular oxygen (15) (16) and remains fully functional after secretion by bacteria (17) (18). FAST allowed also the design of allosteric-like fluorescent reporters for monitoring intracellular analytes (19) and the generation of a fluorescent split reporter enabling the monitoring of protein-protein interactions with unprecedent spatial and temporal resolution (20). In order to provide biologists with a general tool applicable to a broader variety of experimental scenario, we sought to engineer a promiscuous protein tag able to generate a set of chemogenetic reporters having optical properties spanning the entire visible spectrum and attributes suitable for the most advanced imaging techniques. The challenge in designing such a multifunctional protein tag was to find a palette of fluorogenic chromophores that could all be recognized by a single engineered promiscuous binding pocket, and thus easily generate a collection of innovative chemogenetic reporters with multiple properties and optical characteristics for cutting-edge applications in cellular imaging (**Fig. 1a-c**).

Results

Design of fluorogenic chromophores with various spectral properties.

With the aim of obtaining fluorescent assemblies emitting blue, cyan, green, yellow, orange and red light, we explored push-pull chromophores with a broad variety of electronic (and thus spectral) properties by replacing the electron-withdrawing rhodanine (R) heterocycle found in HBR derivatives with pseudothiohydantoin (P), 2,4-thiazolidinedione (T) and 2,4-oxazolidinedione (O), and by secondly varying the substituents on the electron-donating phenol (See **Fig. 1a** for structures). Just like HBR analogs (14), HBX (X = P, T or O) compounds are mainly protonated at physiological pH (their pK_As range from 8.15 to 9.05) (**Fig. S1**), they undergo a significant absorption red-shift upon deprotonation (**Fig. S1**), and they are essentially non-fluorescent in solution. Preliminary screening showed that FAST was able to bind all chromophores, albeit with low to modest affinity (**Table S1**). Like HBR analogs, the HBX (X = P, T or O) analogs displayed red-shifted absorption when bound to FAST at physiological pH (**Table S1**), suggesting that the binding pocket of FAST stabilizes their deprotonated phenolate state in a similar fashion. The corresponding bimolecular assemblies were all fluorescent, although in average dimmer than those formed with the HBR analogs, with absorption/emission peaks blue-shifted by ~35/40 nm (for X = P), ~65/65 nm (for X = T) and ~85/75 nm (for X = O) relative to their HBR-based counterpart. In a given series, changing the number and/or nature of the substituents present on the phenol moiety allowed us furthermore to vary the absorption/emission peaks of the FAST assemblies, as previously observed within the HBR series (21) (**Fig. 1**, **Table S1**).

Engineering of promiscuous FAST variants

With this palette of chromophores at hand, we sought to engineer promiscuous FAST variants able to bind all of them efficiently. Because the chromophores of the HBR, HBP, HBT and HBO series were structurally related, we hypothesized that mutations able to increase the binding affinity and brightness for one chromophore could be sufficient to generate a promiscuous variant displaying improved properties with all chromophores. Directed protein evolution coupled with rational design have previously been an efficient method to generate FAST variants forming bright assembly with new chromophore (22) or having orthogonal chromophore specificity (23). We thus used a combinatorial library of variants generated by random mutagenesis and displayed on yeast cells. Iterative rounds of fluorescence activated cell sorting (FACS) decreasing progressively chromophore concentrations through rounds allowed us to identify variants forming tighter and brighter assemblies with chromophores of the HBX series (**Fig. 2a-d**, **Text S1**, **Fig. S2-S4**, **Tables S2-S9**). Beneficial mutations were combined to generate oFAST, a variant with the mutations Q41L, D71N, V83I, M109L and S117R, which forms a blue fluorescent assembly with HBO-3,5DM 11-fold tighter and 3-fold brighter than FAST:HBO-3,5DM (**Fig. 2b**, **Table S2**). In parallel, the genes of five variants displaying improved properties with HBP-3,5DM were recombined by DNA shuffling to generate a new library (library B, **Fig. 2a**). FACS screening allowed us to identify (i) tFAST, a variant with the mutations G25R, Q41K, S72T, A84S, M95A, M109L and S117R relative to FAST, which forms a cyan fluorescent assembly with HBT-3,5DM 5-fold tighter and 1.5-fold brighter than FAST:HBT-3,5DM (**Fig. 2c**, **Table S3**), and (ii) an improved variant for HBP-3,5DM bearing the mutations K17N, G21E, G25R, A30V, Q41L, S72T, V83A, M95T, S117R, which gave, after addition of the mutation M109L found in several other selected variants, the variant pFAST able to form a green fluorescent assembly with HBP-3,5DM 25-fold tighter and 2.5-fold brighter than FAST:HBP-3,5DM (**Fig. 2d**, **Table S4**).

The variants oFAST, tFAST and pFAST showed superior properties not only with the chromophore used for their selection, but with all chromophores of the HBO, HBT and HBP series, demonstrating that our strategy successfully generated variants with increased chromophore-binding promiscuity. Unlike FAST, the three selected variants bind most of the chromophores of the HBO, HBT and HBP series with submicromolar affinity (**Fig. 2h, Tables S2-S4**). This gain in affinity was accompanied with an increase of the fluorescence quantum yield of almost all fluorescent assemblies (**Fig. 2h, Tables S2-S4**). The three variants displayed also an improved affinity (up to one order of magnitude) for the chromophores of the HBR series, in agreement with an increase of the chromophore binding promiscuity (**Fig. 2h, Tables S2-S4**).

Of the three selected variants showing superior performance, pFAST emerged as the best, and was thus tested with other chromophores. pFAST was shown to form tighter assemblies with HBR analogs bearing an additional carboxymethyl group on the rhodanine head (HBRAA series, **Fig. 1** and **Table S4**). These chromophores were previously shown to have a reduced cellular uptake because of their negatively charged carboxylate at physiological pH, allowing the specific labeling of FAST-tagged proteins located at the cell surface (24). In particular, we discovered that pFAST could efficiently interact with the unreported HBRAA-3,5DM, forming a bright orange fluorescent assembly that was 2.5-fold brighter than FAST:HBRAA-3E, the most efficient combination for selective labeling of cell surface proteins reported so far (24). Finally, we discovered that pFAST could also bind substituted 4-hydroxybenzyldidene isorhodanine derivatives (HBIR series, **Fig. 1**) with single or double digit nanomolar affinities (**Table S4**). The resulting assemblies exhibited red-shifted absorption and emission compared to their HBR counterparts. However, only the red fluorescent pFAST:HBIR-3,5DOM assembly exhibited a decent fluorescent quantum yield: the assemblies with HBIR-3M and HBIR-3,5DM, although among the tightest observed in this study, almost did not fluoresce. Although these properties would disqualify HBIR-3M and HBIR-3,5DM for fluorescence imaging applications, they allowed the efficient generation of absorbing-only dark assemblies (vide infra).

Overall, this set of experiments demonstrated that the selected pFAST was a highly promiscuous protein tag able to bind with high affinity a large variety of structurally related chromophores with diverse electronic properties. Our expanded collection of chromophores allowed the efficient generation of a palette of non-fluorescent and fluorescent assemblies emitting blue, cyan, green, yellow, orange, and red light using a single protein tag (**Fig. 1a-c**, **Fig. S5**).

Structural model

Primary sequence alignments showed that the mutations K17N, G21E, G25R, A30V, Q41L, S72T, V83A, M95T, M109L, S117R found in pFAST were mutation hotspots found in other variants (**Fig. S3**). To get insights into the functional role of these mutations, atomic-resolution models of FAST and pFAST were generated by homology modeling using the tridimensional crystal structure of the evolutionary

related photoactive yellow protein (PYP) from *Halorhodospira halophila* as template (**Fig. 3a** and **Fig. S6a**). The analysis of the root mean square fluctuation (RMSF) of each residue during molecular dynamic simulations showed an overall rigidification of the structure of pFAST compared to FAST (**Fig. 3a,b**). In particular, the loop 94-101 originally mutated to generate FAST from PYP, shows very little movement within pFAST compared to FAST. This overall rigidification was accompanied by a significant reduction of the accessible binding site volume compared to FAST and PYP (**Fig. S6a,b**). All mutations found in pFAST participate to the rigidification of the overall structure and/or in the stabilization of the protein-chromophore assembly. The mutations G21E, G25R introduce two polar residues at the protein surface, which improves the solvation of the protein and thus the compacity of the structure (**Fig. S6e,f**). The mutations A30V and Q41L enable strong hydrophobic interactions with residues in the N-terminal domain, known to be flexible in PYP, and thus play a major role in compacting and rigidifying the entire three-dimensional structure (**Fig. S6g,h**). The mutation S72T creates interactions with the residues Glu 74, Phe75, Tyr76, which have a direct impact on the binding site structure (**Fig. S6i**). The mutation V83A enables closer contacts with the residues Phe79, Ser85, Gly86, Arg87 and Tyr 118, strengthening core interactions (**Fig. S6j**). The mutation M95T strengthens the C-terminal β-sheet through additional interactions with Lys104 and Pro102 (**Fig. S6k**). The mutation M109L directly impacts the size of the binding site by creating hydrophobic interactions with Phe75 and Val120 (**Fig. S6l**). Finally, the mutation S117R participates to the overall rigidification of the structure by creating polar interactions with Asp34 in the N-terminal domain and apolar interactions with Ala112, strengthening the β-sheet structure (**Fig. S6m**). The overall rigidification of pFAST structure creates a chromophore binding site that is smaller, but more open and better defined (**Fig. S6**). Chromophore docking showed that (i) all chromophores of the HBO, HBT, HBP and HBR series could adopt a quasi-planar conformation within the binding site (**Fig. 3c**, **Fig. S6n**), in agreement with bright fluorescent protein-ligand assemblies, and that (ii) pFAST was able to bind all chromophores with higher affinities than FAST does, as observed experimentally (**Fig. S6c**). Our model showed that the conserved residues Tyr42, Glu46, Thr50 and Arg52 form an hydrogen-bound network stabilizing the ground-state deprotonated phenolate in the same way that PYP does with its chromophore, explaining thus the binding-induced red-shift in absorption observed experimentally (25) (26) (27) (28) (**Fig. 3c, Fig. S6n**). In particular, Glu46 forms a strong hydrogen bond with the phenol part of the chromophore, while Arg52 interacts with the electron-withdrawing heterocycle through hydrogen bonding with the endocyclic heteroatom (**Fig. 3c** and **Fig. S6n**). Our model showed that Trp94 and Pro97, known to be essential for chromophore recognition and activation (14), form hydrogen bound and apolar interactions with the chromophore. Fine analysis with HBP-3,5DM allowed us to map the entire network of polar and apolar interactions involved in chromophore recognition and activation (**Fig. 3c**).

Multicolor fluorescent labeling in mammalian cells

Preliminary experiments showed that incubation with the new fluorogenic chromophores for 24 hours had no deleterious effects on mammalian cells at the concentrations used for labeling (**Fig. S7**) and that the expression of the selected variants in mammalian cells was homogenous, in agreement with high intracellular stability (**Fig. 2e-g**). Imaging of live HeLa cells expressing pFAST fused to the histone H2B and treated for few tens of seconds with the different membrane permeant fluorogenic chromophores demonstrated that pFAST could be used to efficiently encode blue, cyan, green, yellow, orange and red fluorescence in mammalian cells (**Fig. 4a**). All chromophores showed good to excellent performances for high-contrast imaging, except HBO-3,5DM and HBO-3M that formed dimmed blue fluorescent assemblies in agreement with their *in vitro* properties. Fluorescence quantification after labeling in both live and fixed cells enabled to show that fixation with paraformaldehyde did not alter significantly fluorescence, suggesting that pFAST remained functional after fixation and could still be labeled (**Fig. S8**). We observed in particular that signal to background ratio in live and fixed cells did not significantly change no matter the chromophore used (**Fig. S8**).

We next showed that selective labeling of cell-surface pFAST-tagged proteins could be efficiently achieved with the membrane impermeant HBRAA-3M, HBRAA-3E and HBRAA-3,5DM. In agreement with the low cell uptake of these three chromophores, labeling of a secreted transmembrane fusion with a pFAST domain facing the extracellular space led to a fluorescence signal restricted at the plasma membrane (**Fig 4a**, **Fig. S9**). We observed that pFAST outperformed FAST in terms of effective brightness in cells, and that HBRAA-3,5DM was the best candidate for the efficient labeling of pFAST-tagged cell-surface proteins, in agreement with its superior in vitro brightness.

Photostability

Continuous chromophore exchange can reduce the apparent rate of photobleaching through renewal of photodamaged chromophores. Photooxidation of specific methionine and tryptophan residues was

however previously shown to cause FAST photodamage (29). Long-term irradiation of live HeLa cells expressing pFAST showed that pFAST displayed enhanced photostability with HMBR, HBR-3,5DM and HBR-3,5DOM, reaching photostability has high as the highly photostable enhanced GFP (EGFP) (**Fig. S10a**). The mutations M95T and M109L may explain the higher photoresistance of pFAST compared to FAST. Prolonged imaging in presence of HBP-3,5DM, HBP-3,5DOM, HBP-3M and HBT-3,5DOM showed that pFAST exhibited also good photostability with these new fluorogenic chromophores, although a rapid transient fluorescence decay was observed before reaching steady state with the last three (**Fig. S10**). Initial fluorescence could be fully recovered in the dark, demonstrating that this initial photobleaching was fully reversible. Decreasing light intensities or reducing imaging frequency enabled furthermore to reduce the amplitude of the initial fluorescence drop. This set of experiments suggested that the observed reversible photobleaching was likely due to photoisomerization and/or photoejection of the chromophore, as previously proposed to explain the reversible photobleaching observed when labeling FAST and its variants with low concentrations of HBR derivatives (29) (23). This singular photochemical signature might be used advantageously for selective imaging techniques based on kinetic discrimination (30) (31) or for single-molecule localization microscopies (32) (33).

Imaging fusion proteins in mammalian cells and cultured neurons

To verify that pFAST was well suited for the selective imaging of proteins in various cellular localizations, HeLa and HEK293T cells expressing pFAST fused to the histone H2B (H2B-pFAST), the mitochondrial targeting sequence from the subunit VIII of human cytochrome C oxidase (Mito-pFAST), the inner plasma membrane targeting sequence lyn11 (Lyn11-pFAST), the actin binding peptide LifeAct (LifeAct-pFAST) and the microtubule-associated protein (MAP) 4 (MAP4-pFAST) were imaged by confocal microscopy in the presence of HBP-3,5DM. pFAST fusions showed proper cellular localization both in live and fixed cells, demonstrating that pFAST did not perturb protein functions (**Fig. 4b**, **Fig. S11** and **Fig. S12**). The high performance of pFAST further allowed us to generate high resolution three-dimensional reconstructions of live HeLa cells expressing lyn11-pFAST from 81 optical sections (**Fig. 4c**) showing the filopodia decorating plasma membrane contours.

To verify the suitability of pFAST for imaging proteins in delicate and sensitive cells, we next expressed FAST fusions in dissociated hippocampal neurons. Dissociated hippocampal neurons were successfully transfected with plasmids encoding Lyn11-pFAST, LifeAct-pFAST or MAP4-pFAST. Live-cell confocal imaging showed (i) that labeled neurons remained fully viable with an impressive transfection rate (**Fig. S13**), in agreement with neither pFAST fusions nor the fluorogenic chromophore being toxic, and (ii) that fusion proteins were properly localized (**Fig. 4d**). As observed for mammalian cells, pFAST allowed us to generate high-resolution confocal micrographs of live neurons (**Fig. 4d**) showing tiny but resolved protrusions, further demonstrating the high brightness and performance of pFAST for live imaging.

Enhanced fluorescent labeling in multicellular organisms

Mechanistic studies of most biological processes require imaging in multicellular organisms. Imaging of semisynthetic chemogenetic reporters in multicellular organisms is however often hampered by the low cell permeability of synthetic probes. HBR derivatives have been previously shown to allow the labeling of FAST and its derivatives in zebrafish embryos thanks to their very high cell uptake and superior ability to diffuse across multicellular systems (14) (22) (23). Preliminary experiments in which we quantified the labeling efficiency in live HeLa cells by flow cytometry showed that full labeling of pFAST was achieved at lower chromophore concentrations than FAST, in agreement with its superior binding affinity (**Fig. S14**), thus facilitating intracellular labeling and minimizing the amount of chromophore required for efficient detection. To verify that pFAST outperformed FAST in a similar fashion for imaging proteins in multicellular organisms, we compared the relative labeling efficiency of pFAST and FAST with various fluorogenic chromophores in chicken embryo. Comparison was performed in the same embryo by expressing each protein in a different side of the neural tube. Time-lapse imaging allowed us to monitor simultaneously the labeling of pFAST and FAST upon successive addition of chromophore solutions with gradually increased concentrations (**Fig. S15**, **Movie S1**). With all tested chromophores, pFAST reached full labeling at lower concentrations than FAST. Fluorescence saturation was furthermore reached within few tens of minutes, in agreement with the high cell uptake of the tested chromophores. The effective brightness of pFAST was in general comparable or higher than that of FAST, further demonstrating the superiority of pFAST over FAST for labeling proteins into tissue (**Fig. S15**).

Encouraged by its superior performance in multicellular organisms, we next compared pFAST with the cyan fluorescent protein mCerulean, the green fluorescent protein EGFP, the yellow fluorescent protein EYFP and the orange fluorescent protein mKO. Direct comparisons were performed within the same embryo by expressing selectively each reporter in a different side of the neural tube. Apart from

pFAST:HBP-3M that displayed lower effective brightness than mCerulean, as expected from their relative molecular brightness, all the other pFAST:chromophore combinations showed performances comparable with those of their fluorescent protein spectral equivalent (**Fig. 5a-g**, **Fig. S16**).

Next, we demonstrated that pFAST was perfectly well suited for imaging proteins involved in dynamic cellular processes within the neuroepithelium of proliferating chicken neural tube by en-face time-lapse multi-color imaging. Tagging mitochondria with Mito-pFAST (labeled with HBR-3,5DOM) and membranes with iRFP670 (memb-iRFP670) allowed us to successfully visualize symmetrical mitochondrial segregation during cell division (**Fig. 5h**, **Movie S2**). Expression of (i) H2B-pFAST (labeled with HBP-3,5DOM), and the PACT domain of pericentrin fused to mKO (pact-mKO) and (ii) H2B-pFAST (labeled with HMBR), pact-mKO, and memb-iRFP670 enabled us on the other hand to visualize chromosome segregation and centromere dynamics during cell division (**Fig. 5i,j**, **Movies S3-S4**). Beyond demonstrating that pFAST was well suited to image dynamic processes in living organisms, this set of experiments also illustrates how the spectral properties of pFAST can be fine-tuned at will by using the most appropriate chromophore for a given experiment.

Overall, these experiments demonstrated that pFAST allowed mechanistic studies of biological processes in multicellular organisms.

Reversible labeling

Some experiments require one to rapidly switch off fluorescence of a given fluorescent reporter. As FAST labeling is non-covalent, it has been previously shown that washing away the fluorogenic chromophore by perfusing chromophore-free medium can reverse the labeling of FAST-tagged proteins in cells and switch off fluorescence with an unprecedented simplicity. As HBIR-3M forms a non-fluorescent assembly with pFAST, we wondered if it could be used as a dark competitor capable of turning off pFAST fluorescence through simple addition to the cell culture medium. Addition of an excess of HBIR-3M proved to efficiently reverse the labeling of pFAST in mammalian cells within just few seconds without the need to wash away the fluorogenic chromophore beforehand (**Fig. S17**, **Movies S5**). Because of its single digit nanomolar binding affinity, HBIR-3M was able to efficiently replace fluorogenic chromophores binding pFAST with low, intermediate and even high affinities. Encouraged by these results, we next tested if HBIR-3M could allow one to switch off pFAST fluorescence in multicellular systems, in which unlabeling by washing is more challenging. Chicken neural tubes expressing H2B-pFAST were dissected and labeled with fluorogenic chromophores. After removal of the excess of chromophore, and washing with phosphate buffer, samples were treated with HBIR-3M and simply washed a second time. While simple washing was unsuccessful to switch off fluorescence, addition of an excess of HBIR-3M efficiently switched off pFAST within few tens of minutes (**Fig. S18**, **Movie S6**). Compared to protocols based on sequential washing steps, unlabeling through addition of a dark competitor can be a very simple and effective method to switch off fluorescence with unprecedented time resolution, in particular when slow passive diffusion prevents efficient washing in cells and multicellular organisms.

pFAST enables imaging with advanced microscopy and nanoscopy

Encouraged by the superior performance of pFAST, we further tested pFAST together with advanced confocal microscopy techniques. Airyscan confocal imaging is a powerful tool allowing the imaging of biological structures in live cells with enhanced signal-to-noise ratio and increased spatial resolution (up to 140 nm). Airyscan confocal imaging of live HeLa cells expressing Lyn11-pFAST or MAP4-pFAST labeled with various HBR or HBP derivatives allowed us to visualize details unresolved by traditional confocal microscopy (**Fig. S19**). Airyscan imaging in live cells allowed us to image the rapid dynamics of microtubules and membranes with high temporal and spatial resolution (**Movie S7**).

We extended our study to Stimulated Emission Depletion (STED) nanoscopy. STED microscopy is a powerful technique allowing the imaging of biological structures in fixed and live cells with nanoscale resolution. As many super-resolution microscopy techniques, the impact of STED nanoscopy is however limited by the number of compatible fluorophores. In STED, a red-shifted doughnut-shaped STED pulse featuring zero intensity at the very center is applied immediately after the excitation pulse, resulting in depletion of the excitation state of the fluorophores within the doughnut area by stimulated emission. Maximal resolution is obtained with bright and photostable fluorophores that are highly sensitive to the STED laser for efficient depletion, and that are not re-excited by it (34). Among our extended palette of chromophores, HBR-3,5DOM appeared well suited for STED as it allowed the generation of a bright and photostable red fluorescent reporter with a 80 nm Stokes shift (Excitation / Emission peaks at 520 nm / 600nm) that allows effective depletion using the common 775 nm pulsed depletion laser while minimizing reexcitation. Labeling with HBR-3,5DOM allowed the imaging of Lyn11-pFAST and MAP4-pFAST in live HeLa cells with nanoscale resolution (**Fig. 6a-e**). pFAST:HBR3,5DOM was bright and

photosable enough to resist multiple average acquisition (16 average line). **Fig. 6a-c** show STED image (b) and deconvoluted STED image (c) compared to confocal (a) and illustrate how STED microscopy allowed us to resolve different filopodia structures (see zoom in) on live samples with the use of bright and photostable pFAST:HBR-3,5DOM. Having at hand a chromophore with spectroscopic properties compatible for STED nanoscopy allowed us to successfully image pFAST fusions below the diffraction barrier in live dissociated hippocampal neurons. Labeling actin with LifeAct-pFAST enabled us to resolve details of axons and dendrites, as well as visualize neurite growth cones with super-resolution (**Fig. 6f-i**). Similarly, targeting microtubule with MAP4-pFAST allowed us to image the microtubule network within live astrocytes with subdiffraction resolution (**Fig. 6j-l**). Overall this set of experiments highlighted the potential of pFAST:HBR3,5DOM for imaging proteins in live cells, including fragile neurons, with sub-diffraction resolution by STED nanoscopy.

Discussion

Fluorescent chemogenetic reporters combine the targeting selectivity of genetic tags with the advantages of synthetic organic fluorophores. Beyond overcoming some of the limitations of traditional fluorescent proteins, these reporters open new ways to image fusion proteins and biochemical processes with high spatial and temporal resolution. We recently developed FAST, a small protein tag of 14k Da (125 amino acid residues) able to bind and activate the fluorescence of HBR derivatives, which are otherwise dark in solution. Here we report the successful engineering of a promiscuous tag, named pFAST, able to recognize a large collection of chromophores, and to form tight bimolecular assemblies with optical properties spanning the entire visible spectrum. Substitutions of few heteroatoms within the chromophore's electron-withdrawing heterocycle allowed us to fine tune the spectral properties with minimal structural changes. A massive engineering effort mostly conducted by directed evolution further enabled us to develop a versatile tag showing good-to-excellent binding/spectroscopic properties with the entire set of fluorogenic compounds. pFAST was evolved from FAST via a rapid and easy-to-implement fluorescence screening strategy based on yeast-display and FACS, further supporting the power of molecular evolution. In agreement with an increase of the chromophore binding promiscuity, pFAST showed improved properties with the chromophores originally developed for FAST. In particular, efficient labeling in cells and in multicellular organisms can be achieved at lower chromophore concentration because of a gain in binding affinity, while longer or more power-demanding imaging experiments can be performed thanks to superior photostability.

The extended chromophore promiscuity of pFAST provides an unprecedented experimental versatility, allowing investigators to face a large variety of experimental scenarios. The panoply of spectrally distinguishable chromophores enables to fine tune pFAST spectral properties to optimize multicolor imaging. Selective labeling of cell-surface pFAST-tagged proteins can be efficiently achieved using bright membrane-impermeant fluorogenic chromophores. The discovery of chromophores forming tight absorbing-only dark assemblies provides moreover new opportunities to control the fluorescence state of pFAST. In particular, the possibility to replace bright chromophores with dark ones by direct competition for the binding site allows one to switch off pFAST fluorescence in cells with an unprecedented time resolution. The ability to form dark complexes absorbing in the green region opens furthermore interesting prospects for the design of dark acceptors for Förster resonance energy transfer (FRET) measurements based on fluorescence lifetime imaging microscopy (FLIM). Like Shadow Green and Yellow, dark acceptors previously engineered from GFP-like proteins (35) (36), pFAST labeled with a dark chromophore could find applications as dark acceptor to modulate the fluorescence lifetime of a donor without blocking an imaging channel. The use of a chemogenetic system such as pFAST has the additional advantage to allow measurements in presence and absence of the acceptor by addition or not of the ligand, and this in a single experiment, eliminating the need for acceptor-free control experiments.

Our study demonstrates that pFAST was perfectly suited to image fusion proteins in live and fixed mammalian cells, including delicate cells such as primary cultured neurons, and in multicellular organisms such as chicken embryo. We show moreover that pFAST can be used to follow dynamic processes in real-time in cells and in embryo tissues.

Finally, we demonstrated that pFAST enabled the imaging of structures below the diffraction barrier in live mammalian cells and live cultured neurons using 3D STED nanoscopy, which broad use is currently limited by the low numbers of fluorophores displaying compatible spectral properties and photostability. The labeling of pFAST with HBR-3,5DOM allowed the successful imaging of membranes, microtubules and actin filaments with sub-diffraction resolution. Beyond applications in STED nanoscopy, we anticipate that a complete and systematic study of the on-off fluorescence blinking or

photoswitching behaviors of pFAST could open new prospects for other advanced imaging techniques, such as single-molecule tracking and super-resolution microscopy by single-molecule localization microscopy (33) (37) (38) or selective imaging exploiting the photokinetic dynamics of fluorescent probes (30) (31).

Materials and Methods

Organic synthesis

General

Commercially available reagents were used as obtained. ^{1}H and ^{13}C NMR spectra were recorded at 300 K on a Bruker AM 300 spectrometer; chemical shifts are reported in ppm with protonated solvent as internal reference ^{1}H, $CHCl_3$ in $CDCl_3$ 7.26 ppm, CHD_2SOCD_3 in CD_3SOCD_3 2.49 ppm, CHD_2COCD_3 in CD_3COCD_3 2.05 ppm; ^{13}C, $^{13}CDCl_3$ in $CDCl_3$ 77.0 ppm, $^{13}CD_3SOCD_3$ in CD_3SOCD_3 39.7 ppm, $^{13}CD_3COCD_3$ in CD_3COCD_3 29.9 ppm; coupling constants J are given in Hz. Mass spectra (chemical ionization and electronic impact with NH_3 or CH_4) were performed by the Service de Spectrométrie de Masse de Chimie ParisTech and mass spectra high resolution were performed by the Service de Spectrométrie de Masse de l'Institut de Chimie Organique et Analytique (Orléans). The preparation of HMBR (4-hydroxy-3-methylbenzylidene rhodanine), HBR-3,5DM (4-hydroxy-3,5-dimethylbenzylidene rhodanine), HBR-3,5DOM (4-hydroxy-3,5-dimethoxybenzylidene rhodanine), HBRAA-3M ((5-(4-hydroxy-3-methylbenzylidene)-4-oxo-2-thioxothiazolidin-3-yl)acetic acid) and HBRAA-3E (5-(4-hydroxy-3-ethylbenzylidene)-4-oxo-2-thioxothiazolidin-3-yl)acetic acid) were previously described (14) (21) (24). The starting compound oxazolidinedione was obtained according to previously described methods (39).

HBP-3M ((4-hydroxy-3-methylbenzylidene)-2-iminothiazolidin-4-one). Solid 4-hydroxy-3-methylbenzaldehyde (130 mg, 1.0 mmol) and pseudothiohydantoin (69 mg, 0.6 mmol) were mixed and the mixture was brought to 170°C. It first fused and then solidified. After cooling to 50-60°C, ethanol was added and the mixture was heated at reflux. The solid partially disintegrated and formed a suspension. It was filtered and the remaining powder was dissolved in 1 M sodium hydroxide. The resulting solution was stirred for 5-10 min and was then slowly acidified with 1 M hydrochloric acid. After cooling to 0°C, the precipitate was filtered, washed with cold water and dried over P_2O_5. HBP-3M was obtained as an orange powder (42 %, 58 mg). ^{1}H NMR (300 MHz, DMSO-d6, δ): 10.03 (s, 1H), 9.28 (s,1H), 9.00 (s,1H), 7.74 (s, 1H), 7.30 (d, 1H, J = 2.0 Hz), 7.24 (dd, 1H, J = 8.3 Hz, 2.0 Hz), 6.92 (d, 1H, J = 8.3 Hz), 2.16 (s, 3H); ^{13}C (75 MHz, DMSO-d6, δ): 180.7, 175.4, 157.2, 132.2, 129.6, 128.9, 125.0, 124.8, 124.7, 115.3, 16.0; HRMS (ESI): m/z 235.0537 (calcd mass for $C_{11}H_{11}N_2O_2S$ $[M+H]^-$ = 235.0536.).

HBP-3,5DM ((4-hydroxy-3,5-dimethylbenzylidene)-2-iminothiazolidin-4-one). As HBP-3M using 4-hydroxy-3,5-dimethylbenzaldehyde (207 mg, 1.4 mmol) and pseudothiohydantoin (100 mg, 0.86 mmol). HBP-3,5DM was obtained as a dark orange powder (83 %, 177 mg). ^{1}H NMR (300 MHz, DMSO-d6, δ): 9.27(s,1H), 8.97(s,1H) ,8.93 (s, 1H),7.42 (s, 1H), 7.16(s, 2H), 2.20 (s, 6H); ^{13}C NMR (75 MHz, DMSO-d6, δ): 180.6, 175.4, 155.1, 130.1 (2C), 129.7, 125.2, 124.9 (2C), 16.7; HRMS (ESI): m/z 249.0694 (calcd mass for $C_{12}H_{13}N_2O_2S$ $[M+H]^-$ = 249.0692.).

HBP-3,5DOM ((4-hydroxy-3,5-dimethoxybenzylidene)-2-iminothiazolidin-4-one). As HBP-3M using 4-hydroxy-3,5-dimethoxybenzaldehyde (251 mg, 1.4 mmol) and pseudothiohydantoin (100 mg, 0.86 mmol). HBP-3,5DOM was obtained as an orange powder (61 %, 146mg). ^{1}H NMR (300 MHz, DMSO-d6, δ): 9.31 (s,1H), 9.10 (s,1H), 9.03 (s,1H), 7.53 (s,1H), 6.88 (s,2H), 3.82 (s,6H); HRMS (ESI): m/z 281.0590 (calcd mass for $C_{12}H_{13}N_2O_4S$ $[M+H]^-$ = 281.0591 (in accordance with previously described analysis (40)).

HBT-3M ((4-hydroxy-3-methylbenzylidene)thiazolidine-2,4-dione). Solid 4-hydroxy-3-methylbenzaldehyde (187 mg, 1.4 mmol) and 2,4-thiazolidinedione (100 mg, 0.85 mmol) were mixed and the mixture was brought to 170°C. It first fused and then solidified. After cooling to 50-60°C, ethanol was added to the solid and the suspension was stirred at reflux until complete dissolution. Then an excess of water was slowly added. The resulting precipitate was filtered, washed with water, and dried over P_2O_5. HBT-3M was obtained as a green powder (55 %, 110 mg). ^{1}H NMR (300 MHz, DMSO-d6, δ): 12.43 (s, 1H), 10.23 (s, 1H), 7.65 (s, 1H), 7.33(d, 1H, J = 2.0 Hz), 7.29 (dd, J = 8.3, 2.0 Hz, 1H), 6.92

(d, J = 8.3 Hz, 1H), 2.16 (s, 3H); ^{13}C NMR (75 MHz, DMSO-d6, δ): 168.2, 167.6, 158.2, 133.2, 132.5, 129.8, 125.2, 123.8, 118.7, 115.4, 15.9; HRMS (ESI): m/z 236.0376 (calcd mass for $C_{11}H_{10}NO_3S$ $[M+H]^-$: 236.0376).

HBT-3,5DM ((4-hydroxy-3,5-dimethylbenzylidene)thiazolidine-2,4-dione). As HBT-3M using 4-hydroxy-3,5-dimethylbenzaldehyde (205 mg, 1.4 mmol) and 2,4-thiazolidinedione (100 mg, 0.85 mmol). HBT-3,5DM was obtained as a yellow powder (75 %, 154 mg). ^1H NMR (300 MHz, DMSO-d6, δ): 12.43 (s, 1H), 9.14 (s, 1H), 7.61 (s, 1H), 7.18 (s, 2H), 2.20 (s, 6H); HRMS (ESI): m/z 250.0533 (calcd mass for $C_{12}H_{12}NO_3S$ $[M+H]^-$: 250.0532.) (in accordance with previously described analysis (41) (42)).

HBT-3,5DOM ((4-hydroxy-3,5-dimethoxybenzylidene)thiazolidine-2,4-one). As HBT-3M using 4-hydroxy-3,5-dimethoxybenzaldehyde (258 mg, 1.4 mmol) and 2,4-thiazolidinedione (100 mg, 0.85 mmol). HBT-3,5DOM was obtained as a green powder (61 %, 146mg). ^1H NMR (300 MHz, DMSO-d6, δ): 12.48 (s, 1H), 9.33 (s, 1H), 7.71 (s, 1H), 6.89 (s, 2H), 3.81 (s, 6H); ^{13}C (75 MHz, DMSO-d6, δ): 168.5, 167.9, 148.7, 139.1, 133.3, 123.7, 120.1, 108.4, 56.5; HRMS (ESI): m/z 282.0431 (calcd mass for $C_{12}H_{12}NO_5S$ $[M+H]^-$: 282.0431) (in accordance with previously described analysis (41) (43)).

HBO-3M ((4-hydroxy-3-methylbenzylidene)oxazolidine-2,4-dione). A mixture of 4-hydroxy-3-methylbenzaldehyde (100 mg, 0.74 mmol), 2,4-oxazolidinedione (148 mg, 1.5 mmol), and pyrrolidine (60 μL, 0.74 mmol) in ethanol (2 mL) was stirred at reflux for 18 h. After cooling, the mixture was diluted with water. The precipitate was collected by filtration, washed with cold water and dried over P_2O_5. HBO-3M was obtained as an orange powder (48 %, 78mg). ^1H NMR (300 MHz, DMSO-d6, δ): 12.16 (s, 1H), 10.04 (s, 1H), 7.51 (d, 1H, J= 3 Hz), 7.47 (dd, 1H, J= 3, 9 Hz), 6.86 (d, 1H, J= 9 Hz), 6.58 (s, 1H), 2.14 (s, 3H); ^{13}C NMR (75 MHz, DMSO-d6, δ): 165.9, 157.2, 154.3, 137.8, 133.1, 129.9, 124.6, 122.4, 115.1, 109.7, 15.9; HRMS (ESI): m/z 220.060512 (calcd mass for $C_{11}H_{10}NO_4$ $[M+H]^-$ = 220.060434).

HBO-3,5DM ((4-hydroxy-3,5-dimethylbenzylidene)oxazolidine-2,4-dione). As HBO-3M using 4-hydroxy-3,5-dimethylbenzaldehyde (100 mg, 0.66 mmol) , 2,4-oxazolidinedione (134 mg, 1.3 mmol), pyrrolidine (55 μL, 0.66 mmol) in ethanol (2 mL). HBO-3,5DM was obtained as an orange powder (43mg, 28 %). ^1H NMR (300 MHz, DMSO-d6, δ): 12.10 (s, 1H), 8.95 (s,1H), 7.37 (s, 2H), 6.53 (s, 1H), 2.19 (s, 6H); HRMS (ESI): m/z 234.076560 (calcd mass for $C_{12}H_{12}NO_4$ $[M+H]^-$ = 234.076084). (in accordance with previously described analysis (44))

HBIR-3M ((4-hydroxy-3-methylbenzylidene)-4-thioxothiazolidin-2-one). As HBP-3M using 4-hydroxy-3-methylbenzaldehyde (164 mg, 1.2 mmol) and isorhodanine (100 mg, 0.75 mmol). HBIR-3M was obtained as an orange powder (49%, 93 mg). ^1H NMR (300 MHz, DMSO-d6, δ): 10.53 (s, 1H), 8.01 (s, 1H), 7.43 (d, 1H, J = 2.0 Hz), 7.38 (dd, 1H, J = 8.3 Hz, 2.0 Hz), 6.96 (d, 1H, J = 8.3Hz), 2.16 (s, 3H); ^{13}C NMR (75 MHz, DMSO-d6, δ): 194.9, 170.8, 159.2, 137.3, 134.1, 130.8, 125.7, 125.6, 124.4, 115.7, 15.9; HRMS (ESI): m/z 252.014671 (calcd mass for $C_{11}H_{10}NO_2S_2$ $[M+H]^-$ = 252.014747).

HBIR-3,5DM ((4-hydroxy-3,5-dimethylbenzylidene)-4-thioxothiazolidin-2-one). As HBP-3M using 4-hydroxy-3,5-dimethylbenzaldehyde (180 mg, 1.2 mmol) and isorhodanine (100 mg, 0.75 mmol). HBIR-3,5DM was obtained as a brown powder (69%, 137 mg). ^1H NMR (300 MHz, DMSO-d6, δ): 13.66 (s, 1H), 9.39 (s, 1H), 7.97 (s, 1H), 7.28 (s, 2H), 2.21 (s, 6H); ^{13}C NMR (75 MHz, DMSO-d6, δ): 194.9, 170.8, 157.1, 137.2, 131.8, 125.7, 125.5, 124.5, 16.6; HRMS (ESI): m/z 266.030241 (calcd mass for $C_{12}H_{12}NO_2S_2$ $[M+H]^-$ = 266.030397).

HBIR-3,5DOM ((4-hydroxy-3,5-dimethoxylbenzylidene)-4-thioxothiazolidin-2-one). As HBP-3M using 4-hydroxy-3,5-dimethoxybenzaldehyde (220 mg, 1.2 mmol) and isorhodanine (100 mg, 0.75 mmol). HBIR-3,5DOM was obtained as a brown powder (48%, 110 mg). ^1H NMR (300 MHz, DMSO-d6, δ): 13.72 (s, 1H), 9.60 (s, 1H), 8.05 (s, 1H), 6.97 (s, 2H), 3.83 (s, 6H); ^{13}C NMR (75 MHz, DMSO-d6, δ): 194.9, 170.8, 148.3, 139.3, 137.5, 126.5, 123.8, 108.7, 56.1; HRMS (ESI): m/z 298.020265 (calcd mass for $C_{12}H_{12}NO_4S_2$ $[M+H]^-$ = 298.020226) (in accordance with previously described analysis) (45).

HBRAA-3,5DM 5-(4-hydroxy-3,5-dimethylbenzylidene)-4-oxo-2-thioxothiazolidin-3-yl) acetic acid. A solution of rhodanine-3-acetic acid (191 mg, 1.0 mmol) and 4-hydroxy-3,5-dimethylbenzaldehyde (150 mg, 1.0 mmol) in water (70 mL) was stirred at 90°C for 7 days. After cooling to 4°C and standing overnight, the precipitate was filtered through a glass filter and the crude solid was washed with water, ethanol and dried over P_2O_5, to give the desired product as an orange powder (160 mg, 50 %). ^1H NMR

(300 MHz, CD_3SOCD_3, δ): 9.40 (s, 1H), 7.70 (s, 1H), 7.27 (s, 2H), 4.72 (s, 2H), 2.23 (s, 6H); ^{13}C NMR (75 MHz, CD_3SOCD_3, δ): 193.6, 167.8, 166.9, 157.7, 135.3, 132.4(2C), 126.0(2C), 124.3, 117.4, 45.4, 17.1(2C); MS (ESI): m/z 322.2 (calcd mass for $C_{14}H_{12}NO_4S_2$ $[M-H]^-$ = 322.0).

Biology

General

Synthetic oligonucleotides used for cloning were purchased from Integrated DNA technology. PCR reactions were performed with Q5 polymerase (New England Biolabs) in the buffer provided. PCR products were purified using QIAquick PCR purification kit (Qiagen). The products of restriction enzyme digests were extracted and purified by preparative gel electrophoresis followed by QIAquick gel extraction kit (Qiagen). Restriction endonucleases, DNAse I, T4 ligase, Fusion polymerase, Tag ligase and Tag exonuclease were purchased from New England Biolabs and used with accompanying buffers and according to manufacturer protocols. Isothermal assemblies (Gibson assembly) were performed using homemade mix prepared according to previously described protocols (46). Small-scale isolation of plasmid DNA was done using QIAprep miniprep kit (Qiagen) from 2 mL overnight bacterial culture supplemented with appropriate antibiotics. Large-scale isolation of plasmid DNA was done using the QIAprep maxiprep kit (Qiagen) from 150 mL of overnight bacterial culture supplemented with appropriate antibiotics. All plasmid sequences were confirmed by Sanger sequencing with appropriate sequencing primers (GATC Biotech). All the plasmids used in this study are listed in **Tables S10** and **S11**. The protein and DNA sequences of FAST and pFAST are given in **Table S12**.

Yeast display

Library construction. The first yeast library (called library A in this study) of FAST constructed by error-prone PCR using Genemorph II kit (Agilent) was previously described (23)**.** The second library (called library B in this study) was constructed by DNA shuffling according to different DNA shuffling library protocols (47) (48) (49)**.** Five gene variants (with more than 70% of sequences homology) previously screened, selected and rationally designed from the library A were first amplified by PCR. They were randomly digested by DNAse I (20 U/mL). The digested products were purified and mixed together. Two steps of PCR amplification (one without primers and the second one with two primers to amplify the full-length genes) were then performed enabling random recombination and amplification of the full-length shuffled product. In addition, a mutation rate of 4 nt/gene and a deletion rate of 0.25 nt/gene were obtained (as shown by Sanger sequencing of 17 individual clones). The shuffled product was cloned into pCTCON2 using NheI and BamHI restriction sites. Large scale transformation into DH10B was performed, yielding 5.5×10^7 transformants. The DNA was maxiprepped and transformed into yeast strain EBY100 using a large-scale, high-efficiency protocol (50) to yield 6.7×10^7 transformants.

Selection. The yeast library (about 1-5 x 10^9 cells) was grown over night at 30°C in 1L SD medium (20 g/L dextrose, 6.7 g/L yeast nitrogen base, 1.92 g/L yeast synthetic dropout without tryptophan, 7.44 g/L NaH_2PO_4, 10.2 g/L Na_2HPO_4-$7H_2O$, 1% penicillin-streptomycin 10,000 U/mL). The following morning yeast culture was diluted to OD_{600nm} 1 in 1L of SD and grown at 30°C until OD_{600nm} 2-5. Next, 5×10^6 cells were pelleted and resuspended in 1 L of SG medium (20 g/L galactose, 2 g/L dextrose 6.7 g/L yeast nitrogen base, 1.92 g/L yeast synthetic dropout without tryptophan, 7.44 g/L NaH_2PO_4, 10.2 g/L Na_2HPO_4-$7H_2O$, 1% penicillin-streptomycin 10,000 U/mL) to grow for 36 hours at 23°C. 5×10^8 induced yeast cells were collected (2500 × g - 2min) , washed with 10 mL PBS (0.05 M phosphate buffer, 0.150 M NaCl, pH 7.4) + BSA (bovine serum albumin 1 g/L) and incubated for 30 min at room temperature with 1:250 dilution of primary antibody chicken anti-c-myc IgY (Life technologies) in 200 µL of PBS. Cells were then centrifuged, washed with PBS-BSA and incubated for 20min on ice with 1:100 dilution of secondary goat-anti chicken antibody coupled to AlexaFluor 647 in 200 µL of PBS. After centrifugation and washing with 10 mL PBS + BSA, the cells were resuspended in 5 mL of PBS supplemented with appropriate fluorogen concentration. The cells were sorted on a MoFlo™ Astrios Cell sorter (Beckman Coulter) equipped with 405 nm, 488 nm and 640 nm lasers. The fluorescence of HBO-3,5DM and HBO-3M binders were detected using the following parameters: Ex 405 nm, Em 458 ± 30 nm. For the selection using library A, the fluorescence of HBT-3,5DM and HBT-3M binders were detected using the following parameters: Ex 405 nm, Em 488 ± 5 nm. For the selection using library B, the fluorescence of HBT-3,5DM binders was detected using the following parameters: Ex 405 nm, Em 513 ± 13 nm. The fluorescence of HBP-3,5DM and HBP-3M binders were detected using the following parameters: Ex

488nm, Em 526 ± 26 nm. Finally, the fluorescence of HBP-3,5DOM binders was detected using the following parameters: Ex 488 nm, Em 546 ± 10 nm. Sorted cells were collected in SD, grown over night at 30°C and plates on SD plates (SD supplemented with 182 g/L D-sorbitol and 15 g/L agar) for approximately 60 hours at 30°C. The resulting lawn was collected in SD supplemented with 30% glycerol, aliquoted and frozen or directly used for the next round of selection. In total, 5 to 8 rounds of selection were performed for each fluorogen. After each selection, 24 clones per final rounds were isolated, screened by flow cytometry and their plasmidic DNA was isolated using miniprep kit (Qiagen), transformed in DH10B and re-isolated for sequencing.

Cloning. Variants obtained by rational design were cloned in pCTCON2 plasmids driving EBY100 yeast surface expression using NheI and BamHI restriction sites as for library construction *(vide supra)*. All the plasmids used in this study are listed in **Table S10**.

Flow cytometry analysis. Flow cytometry was performed on a Gallios analyzer (Beckman Coulter) equipped with 405 nm, 488 nm and 638 nm lasers and ten filters and channels. To prepare samples for flow cytometry, small scale cultures were grown as for library expression *(vide supra)*. Briefly, 5 mL of SD were inoculated with a single colony and grown overnight at 30°C. The following day, the cultures were diluted in 5 mL of SD to a final OD_{600nm} 1 and grown until OD_{600nm} 2-5. These cultures were used to inoculate 5 mL of either SD (non-induced cultures) or SG (induced cultures) to an OD_{600nm} of 0.5 and the cultures were grown for 36 h at 23°C. The cultures were collected (2500 × g - 2min) to reach a final concentration of 1×10^8 cells/mL. For analysis, the monoclonal yeast cells were prepared and incubated with the set of antibodies as for library expression (vide supra). The cultures were finally resuspended in PBS supplemented with appropriate fluorogens concentrations. Data were analyzed using Kaluza Analysis software (Beckman Coulter).

Characterization of variants

Cloning. Plasmids driving *E. coli* expression of the variants with an N-terminal His-tag under the control of a T7 promoter were constructed by replacing the sequence coding for FAST in the plasmid pAG87 (14) using isothermal Gibson assembly. Site-directed mutagenesis was performed by isothermal Gibson assembly using primers with the mutations of interest. All the characterized variants are listed in **Table S11**.

Expression. The plasmids were transformed in Rosetta (DE3) pLys *E. coli* (New England Biolabs). Cells were grown at 37°C in lysogen Broth (LB) medium supplemented with 50 µg/ml kanamycin and 34 µg/mL chloramphenicol to OD_{600nm} 0.6. Expression was induced overnight at 16°C by adding isopropyl-β-D-1-thiogalactopyranoside (IPTG) to a final concentration of 1 mM. Cells were harvested by centrifugation (4,300 × g for 20min at 4°C) and frozen.

Purification. The cell pellet was resuspended in lysis buffer (PBS supplemented with 2.5 mM $MgCl_2$, 1mM of protease inhibitor PhenylMethaneSulfonyl Fluoride PMSF, 0.025 mg/mL of DNAse, pH 7.4) and sonicated (5 min, 20 % of amplitude) on ice. The lysate was incubated for 2-3 hours on ice to allow DNA digestion by DNAse. Cellular fragments were removed by centrifugation (9,000 × g for 1 h at 4°C). The supernatant was incubated overnight at 4°C by gentle agitation with pre-washed Ni-NTA agarose beads in PBS buffer complemented with 20 mM of imidazole. Beads were washed with 10 volumes of PBS complemented with 20 mM of imidazole and with 5 volumes of PBS complemented with 40mM of imidazole. His-tagged proteins were eluted with 5 volumes of PBS complemented with 0.5 M of imidazole. The buffer was exchanged to PBS (0.05 M phosphate buffer, 0.150 M NaCl) using PD-10 or PD-MidiTrap G-25 desalting columns (GE Healthcare). Purity of the proteins were evaluated using SDS-PAGE electrophoresis stained with Coomassie blue.

Physico-chemical measurements. Steady state UV-Vis absorption spectra were recorded using a Cary 300 UV-Vis spectrometer (Agilent Technologies), equipped with a Versa20 Peltier-based temperature-controlled cuvette chamber (Quantum Northwest) and fluorescence spectra were recorded using a LPS 220 spectrofluorometer (PTI, Monmouth Junction, NJ), equipped with a TLC50TM Legacy/PTI Peltier-based temperature-controlled cuvette chamber (Quantum Northwest). Fluorescence quantum yield measurements were determined as previously described using either FAST:HMBR or quinine sulfate as a reference (14) (21) (51) (23). Reciprocal dilution with protein solution was used so as to keep the protein concentration constant at 40 µM while diluting the fluorogen solution. Absorption coefficients were determined by forward titration of fluorogens into a 40 µM protein solution. Thermodynamic

dissociation constants were determined as previously described (14) using a Spark 10M plate reader (Tecan) and fitting data in Prism 6 to a one-site specific binding model. The thermodynamic dissociation constants (K_D) of the dark HBIR-3M and HBIR-3,5DM chromophores were determined by determining the apparent dissociation constant of HBP-3,5DM in presence of various concentrations of dark competitors (See **Text S2**).

Modeling

Homology modeling. The homology models of FAST and pFAST were generated according to models previously described (52) (53). Briefly, sequence alignments between FAST and pFAST and the ultra-high resolution structure of the *Halorhodospira halophila* Photoactive Yellow Protein (PYP) (Protein Data Bank (PDB) ID: 6P4I) were generated with Clustal W (54). Alignments were manually refined to avoid gaps in predicted (FAST and pFAST) and known (PYP) secondary structure elements. Three-dimensional FAST and pFAST models were built from these alignments and from crystallographic atomic coordinates of PYP using the automated comparative modeling tool MODELER (Sali and Blundell) implemented in Discovery Studio. The best model according to DOPE score (Discrete Optimized Protein Energy) and potential energy calculated by modeler were solvated (10 Å water box and 0.145M NaCl) and minimized using Adopted Basis NR algorithm to a final gradient of 0.001. The resulting structure were submitted to a 10ns NAMD dynamic.

Molecular Docking. Flexible ligand-rigid protein docking was performed using CDOCKER implemented in Discovery Studio 2019 (55). Random ligand conformations were generated from the initial ligand structure through high-temperature molecular dynamics. The best poses according to their ligscore2 (56) were retained and clustered according to their binding mode. The most significant poses were solvated and minimized using Adopted Basis NR algorithm to a final gradient of 0.001.

Experiments in mammalian cell

General. HeLa cells were cultured in Minimal Essential Media (MEM) supplemented with phenol red, Glutamax I, 1 mM of sodium pyruvate, 1% (vol/vol) of non-essential amino-acids and 10% (vol/vol) fetal calf serum (FCS), at 37 °C in a 5% CO_2 atmosphere. HEK 293T cells were cultured in Dulbecco's Modified Eagle Medium (DMEM) supplemented with phenol red and 10% (vol/vol) fetal calf serum at 37 °C in a 5% CO_2 atmosphere. For imaging, cells were seeded in μDish IBIDI (Biovalley) coated with poly-L-lysine. Cells were transiently transfected using Genejuice (Merck) according to the manufacturer's protocol for 24 hours prior to imaging. Live cells were washed with DPBS (Dulbecco's Phosphate-Buffered Saline), and treated with DMEM media (without serum and phenol red) containing the fluorogens at the indicated concentration. The cells were imaged directly without washing. Fixation of cells was performed using formaldehyde solution at 3.7 % for 30 min. Fixed cells were then washed three times with DPBS and treated with DPBS containing the fluorogens at the indicated concentration prior to imaging.

Cloning. The plasmids allowing the mammalian expression of pFAST, tFAST and oFAST variants under the control of a CMV promoter were constructed by replacing the sequence coding for FAST (14) or iFAST (51) in the previously described plasmids pAG104 (FAST), pAG106 (lyn11-FAST), pAG109 (H2B-FAST), pAG156 (mito-FAST), pAG470 (lifeAct-iFAST) and pAG498 (MAP4-FAST) using isothermal Gibson assembly. All the plasmids used in this study are listed in **Table S10**.

Cell viability assay. HeLa cells were treated with MEM media containing the appropriate fluorogen (HBP-3,5DOM, HBP-3,5DM, HBP-3M, HBT-3,5DOM, HBT-3,5DM, HBT-3M, HBO-3,5DM, HBO-3M, HBIR-3,5DOM, HBIR-3,5DM and HBIR-3M) at the indicated concentrations for the indicated times. The cell viability was evaluated by fluorescence microscopy using the LIVE/DEAD® viability/cytotoxicity assay kit (Molecular Probes, Life Technologies) following the manufacturer's protocol.

Fluorescence microscopy. The confocal micrographs of mammalian cells were acquired on a Zeiss LSM 710 Laser Scanning Microscope equipped with a Plan Apochromat 63× /1.4 NA oil immersion objective and on a Leica TCS SP5 confocal laser scanning microscope equipped with a 63×/ 1.4 NA oil immersion objective. ZEN and Leica LAS AF softwares were used to collect the data. Zeiss LSM 880 confocal laser scanning microscope equipped with a 63×/1.4 NA oil immersion objective and equipped with photomultiplier modules for confocal imaging and a dedicated highly sensitive spectral detector using the Airyscan module was used to acquire improved spatial resolution images of HeLa cells. Airyscan

uses a 32-channel gallium arsenide phosphide photomultiplier tube (GaAsP-PMT) area detector that collects a pinhole-plane image at every scan position. Each detector element functions as a single, very small pinhole (57). ZEN blue and black softwares were used to collect the data and processing of Airyscan images were performed on the software. The images were analyzed with Fiji (Image J).

Photobleaching measurements for HBR-3,5DOM, HBR-3,5DM, HMBR, HBP-3,5DOM, HBP-3,5DM and HBP-3M were acquired using 405, 458 and 488 nm excitation in different illumination conditions. At 488 nm excitation, EGFP was used as a control. At 458 nm excitation, mTurquoise2 was used as a control. Samples were acquired continuously for 150 images or 500 images using different time lapse between two images. In all cases the pixel dwell was 2.55 μs. The images were analyzed with Fiji (Image J).

Super resolution microscopy. STimulated Emission Depletion (STED) images were acquired on NeurImag facility with a confocal laser scanning microscope LEICA SP8 STED 3DX equipped with a 93×/1.3 NA glycerol immersion objective and with two hybrid detectors (HyDs). The specimens were imaged with a white-light laser and a pulsed 775 nm depletion laser to acquire nanoscale imaging. Typically, images of 1024×1024 pixels were acquired with a magnification above 3 resulting in a pixel size in the range of 25-45 nm. Deconvolution processing were performed on STED images using CMLE analysis with Huyguens software. Iterative processes (up to 40 cycles) were used with a quality criteria ranging from 1 to 5 percent.

Flow cytometry analysis. Flow cytometry on HEK 293T cells was performed on a Gallios analyzer (Beckman Coulter) equipped with 405 nm, 488 nm and 638 nm lasers and ten filters and channels. To prepare samples, cells were first grown in cell culture flasks, then transiently co-transfected with pAG104 (cmv-FAST) and pAG753 (cmv-iRFP670) or pAG654 (cmv-pFAST) and pAG753 (cmv-iRFP670) 24 hours after seeding, using Genejuice (Merck) according to the manufacturer's protocol for 24 hours. Simple positive controls were also prepared by transiently transfected cells with either pAG753 or pAG654 plasmids. After 24 hours, cells were centrifuged in PBS with BSA (1mg/ml) and resuspend in PBS-BSA supplemented with the appropriate amounts of fluorogens. For each experiments, 20,000 cells positively transfected with iRFP670 (Ex 638 nm / Em 660 ± 10 nm) were analyzed with the following parameters: Ex 488nm, Em 525 ± 20 nm for cells expressing FAST and pFAST labeled with HMBR and HBP-3,5DM ; Ex 488 nm, Em 575 ± 15 nm for cells expressing FAST and pFAST labeled with HBR-3,5DM and HBP-3,5DOM and Ex 488 nm, Em 620 ± 15 nm for cells expressing FAST and pFAST labeled with HBR-3,5DOM. Data were analyzed using Kaluza Analysis software (Beckman Coulter).

Experiments in primary hippocampal neuronal cells

All experiments involving rats were performed in accordance with the directive 2010/63/EU of the European Parliament and of the Council of 22 September 2010 on the protection of animals used for scientific purposes. Hippocampal neurons from embryonic rats (E18) were prepared as described previously (58). Cells were grown on onto poly-L-lysine-coated 18-mm coverslips (1 mg/ml) at a density of 25,000 cells /cm^2 in Neurobasal-B27 medium previously conditioned by a confluent glial feeder layer [Neurobasal medium (ThermoFisher 21103049) containing a 2% B27 supplement (ThermoFisher A3582801), and 500 µM L-glutamine (ThermoFisher 25030024)]. Neurons were transfected 2 days before imaging using Lipofectamin 2000 (ThermoFisher). After 10 to 21 days *in vitro*, neurons were incubated with the fluorogenic chromophores and imaged immediately at 37°C.

Experiments in chicken embryos

JA57 chicken fertilized eggs were provided by EARL Morizeau (8 rue du Moulin, 28190 Dangers, France) and incubated at 38°C in a Sanyo MIR-253 incubator. Embryos used in this study were between E2 (HH14) and E3 (HH14 + 24 h). The sex of the embryos was not determined.

Cloning. For expression of H2B-FAST and H2B-pFAST in the chick neural tube, the CMV promoters in pAG109 and pAG657 and pAG671 were converted to a CAGGS promoter (59) by replacing the NdeI/BglII fragment with a NdeI/BglII CAGGS fragment from pCAGGS-MCS2 (X. Morin, unpublished). For expression of mito-pFAST, the NdeI/EcoRI fragment of the CMV promoter in pAG671 was replaced with the NdeI/EcoRI CAGGS fragment from pCAGGS-MCS2. pCAGGS-H2B-mCerulean was created by removing an SphI fragment from Tol2-CAG::Nucbow (Addgene #158992), and pCAGGS-H2B-EYFP was obtained by removing an AgeI fragment from PB-CAG::CytBow (Addgene #158995). Construction details, complete sequences and plasmids are available upon request.

Electroporation in the chick neural tube was performed at embryonic day 2 (E2, HH stage 14), by applying five pulses of 50 ms at 25 V with 100 ms in between, using a square-wave electroporator (Nepa Gene, CUY21SC) and a pair of 5-mm gold-plated electrodes (BTX Genetrode model 512) separated by a 4-mm interval. The DNA solution was injected directly into the lumen of the neural tube via glass capillaries. Bilateral electroporation was achieved by switching the electrodes polarity and repeating the procedure after 2 hours. DNA constructs were used at 0.5 µg/µl each, except pCX-mbCherry which was used at a concentration of 0.3µg/µl. En-face culture of the embryonic neuroepithelium was performed at E3 (24 h after electroporation). After extraction from the egg and removal of extraembryonic membranes in PBS, embryos were transferred to 37°C F12 medium and pinned down with dissection needles at the level of the hindbrain and hindlimbs in a 35mm Sylgard dissection dish. A dissection needle was used to separate the neural tube from the somites from hindbrain to caudal end on both sides of the embryo, and the roof-plate was then slit with the needle. The neural tube and notochord were then "peeled off" from the remaining tissues and equilibrated 2 min in 1% low meting point agarose/F12 medium at 38°C. The tissue was then transferred in a drop of agarose medium to a glass-bottom culture dish (MatTek, P35G-0-14-C) and excess medium was removed so that the neural tube would flatten with its apical surface facing the bottom of the dish, in an inverted open book conformation. After 30 s of polymerization on ice, an extra layer of agarose medium (100µl) was added to cover the whole tissue and hardened on ice for 1 min. 1.9 mL of 37°C culture medium was added (F12/Penicillin Streptomycin/Sodium pyruvate) and the culture dish was transferred to the 37°C chamber of a spinning disk confocal microscope. To image pFAST and FAST, intermediate dilutions (2 to 200µM) of ligands HBR-3,5DOM, HBR-3,5DM, HMBR, HBP-3,5DOM, HBP-3,5DM, HBP-3M and HBIR-3M were prepared by diluting the original 20mM stocks in F12 medium, and appropriate volumes were added to the dish to reach the desired final concentrations.

Live imaging was performed on an inverted microscope (Nikon Ti Eclipse) equipped with a heating enclosure (DigitalPixel, UK), a spinning disk head (Yokogawa CSUW1) and Borealis system (Andor) for confocal imaging, a Spectra-X LED light engine (Lumencor) for widefield fluorescence illumination and an sCMOS Camera (Orca Flash4LT, Hamamatsu) driven by MicroManager software (60). Image stacks were obtained at 2- or 3-min intervals either with a 10× objective (CFI Plan APO LBDA, NA 0.45, Nikon; z-step = 4 µm) or a 100× oil immersion objective (APO VC, NA 1.4, Nikon; z-step = 1 µm).

Acknowledgments

We thank K. D. Wittrup, for providing us with the pCTCON2 vector and the EBY100 yeast strain for the yeast display selection. We thank the flow cytometry facility CISA (Cytométrie Imagerie Saint-Antoine) of UMS LUMIC at the Faculty of Medicine of Sorbonne Université, and, more particularly, Annie Munier for her assistance. We thank the imaging facility of the Institut de Biologie Paris Seine of Sorbonne Université. Airyscan and STED experiments were carried out at NeurImag Imaging core facility, part of the IPNP, Inserm 1266 unit and Université de Paris. We thank Leducq establishment for funding the Leica SP8 Confocal/STED 3DX system and Sésame Région Ile-de-France for funding the Zeiss 880 Confocal/Airyscan system. This work has been supported by the European Research Council (ERC-2016-CoG-724705 FLUOSWITCH), the Agence Nationale de la Recherche (France BioImaging - ANR-10-INBS-04, Morphoscope2 - ANR-11-EQPX-0029, ANR-19-CE13-0026 ADOBE) and a prematuration grant from PSL University and QLife.

References

1. R. Y. Tsien, The Green Fluorescent Protein. *Annu. Rev. Biochem.* **67**, 509–544 (1998).
2. J. Wiedenmann, F. Oswald, G. U. Nienhaus, Fluorescent proteins for live cell imaging: opportunities, limitations, and challenges. *IUBMB Life* **61**, 1029–1042 (2009).
3. A. Keppler, *et al.*, A general method for the covalent labeling of fusion proteins with small molecules in vivo. *Nat. Biotechnol.* **21**, 86–89 (2003).
4. G. V. Los, *et al.*, HaloTag: a novel protein labeling technology for cell imaging and protein analysis. *ACS Chem. Biol.* **3**, 373–382 (2008).
5. A. Gautier, *et al.*, An Engineered Protein Tag for Multiprotein Labeling in Living Cells. *Chem. Biol.* **15**, 128–136 (2008).
6. Y. Hori, *et al.*, Development of Fluorogenic Probes for Quick No-Wash Live-Cell Imaging of

Intracellular Proteins. *J. Am. Chem. Soc.* **135**, 12360–12365 (2013).
7. C. Szent-Gyorgyi, *et al.*, Fluorogen-activating single-chain antibodies for imaging cell surface proteins. *Nat. Biotechnol.* **26**, 235–240 (2008).
8. J. B. Grimm, *et al.*, A general method to improve fluorophores for live-cell and single-molecule microscopy. *Nat. Methods* **12**, 244–250 (2015).
9. J. B. Grimm, *et al.*, A general method to fine-tune fluorophores for live-cell and *in vivo* imaging. *Nat. Methods* **14**, 987–994 (2017).
10. L. Wang, *et al.*, A general strategy to develop cell permeable and fluorogenic probes for multicolour nanoscopy. *Nat. Chem.* **12**, 165–172 (2020).
11. A. Gautier, A. G. Tebo, Sensing cellular biochemistry with fluorescent chemical–genetic hybrids. *Curr. Opin. Chem. Biol.* **57**, 58–64 (2020).
12. H. Ben Aissa, A. Gautier, Engineering Glowing Chemogenetic Hybrids for Spying on Cells. *Eur. J. Org. Chem.* **2020**, 5637–5646 (2020).
13. F. Broch, A. Gautier, Illuminating Cellular Biochemistry: Fluorogenic Chemogenetic Biosensors for Biological Imaging. *ChemPlusChem* **85**, 1487–1497 (2020).
14. M.-A. Plamont, *et al.*, Small fluorescence-activating and absorption-shifting tag for tunable protein imaging in vivo. *Proc. Natl. Acad. Sci.* **113**, 497–502 (2016).
15. H. E. Streett, K. M. Kalis, E. T. Papoutsakis, A Strongly Fluorescing Anaerobic Reporter and Protein-Tagging System for Clostridium Organisms Based on the Fluorescence-Activating and Absorption-Shifting Tag Protein (FAST). *Appl. Environ. Microbiol.* **85**, e00622-19 (2019).
16. K. Charubin, S. Modla, J. L. Caplan, E. T. Papoutsakis, Interspecies Microbial Fusion and Large-Scale Exchange of Cytoplasmic Proteins and RNA in a Syntrophic Clostridium Coculture. *mBio* **11** (2020).
17. Y. Chekli, *et al.*, Visualizing the dynamics of exported bacterial proteins with the chemogenetic fluorescent reporter FAST. *Sci. Rep.* **10**, 15791 (2020).
18. C. Peron-Cane, *et al.*, Fluorescent secreted bacterial effectors reveal active intravacuolar proliferation of Listeria monocytogenes in epithelial cells. *PLOS Pathog.* **16**, e1009001 (2020).
19. A. G. Tebo, *et al.*, Circularly Permuted Fluorogenic Proteins for the Design of Modular Biosensors. *ACS Chem. Biol.* **13**, 2392–2397 (2018).
20. A. G. Tebo, A. Gautier, A split fluorescent reporter with rapid and reversible complementation. *Nat. Commun.* **10**, 2822 (2019).
21. C. Li, *et al.*, Dynamic multicolor protein labeling in living cells. *Chem. Sci.* **8**, 5598–5605 (2017).
22. C. Li, *et al.*, A Far-Red Emitting Fluorescent Chemogenetic Reporter for In Vivo Molecular Imaging. *Angew. Chem. Int. Ed.* **59**, 17917–17923 (2020).
23. A. G. Tebo, *et al.*, Orthogonal fluorescent chemogenetic reporters for multicolor imaging. *Nat. Chem. Biol.*, 1–9 (2020).
24. C. Li, *et al.*, Fluorogenic Probing of Membrane Protein Trafficking. *Bioconjug. Chem.* **29**, 1823–1828 (2018).
25. T. E. Meyer, *et al.*, Site-Specific Mutations Provide New Insights into the Origin of pH Effects and Alternative Spectral Forms in the Photoactive Yellow Protein from Halorhodospira halophila. *Biochemistry* **42**, 3319–3325 (2003).
26. Y. Imamoto, M. Kataoka, Structure and Photoreaction of Photoactive Yellow Protein, a Structural Prototype of the PAS Domain Superfamily†. *Photochem. Photobiol.* **83**, 40–49 (2007).
27. L. Wei, H. Wang, X. Chen, W. Fang, H. Wang, A comprehensive study of isomerization and protonation reactions in the photocycle of the photoactive yellow protein. *Phys. Chem. Chem. Phys. PCCP* **16**, 25263–25272 (2014).
28. R. Brudler, *et al.*, Coupling of Hydrogen Bonding to Chromophore Conformation and Function in Photoactive Yellow Protein. *Biochemistry* **39**, 13478–13486 (2000).
29. F. M. Pimenta, *et al.*, Chromophore Renewal and Fluorogen-Binding Tags: A Match Made to Last. *Sci. Rep.* **7** (2017).
30. G. Marriott, *et al.*, Optical lock-in detection imaging microscopy for contrast-enhanced imaging in living cells. *Proc. Natl. Acad. Sci.* **105**, 17789–17794 (2008).
31. J. Quérard, *et al.*, Resonant out-of-phase fluorescence microscopy and remote imaging overcome spectral limitations | Nature Communications. *Nat. Commun.* **8**, 969 (2017).
32. J. Kwon, *et al.*, Bright ligand-activatable fluorescent protein for high-quality multicolor live-cell super-resolution microscopy. *Nat. Commun.* **11**, 273 (2020).
33. B. Turkowyd, D. Virant, U. Endesfelder, From single molecules to life: microscopy at the nanoscale. *Anal. Bioanal. Chem.* **408**, 6885–6911 (2016).
34. M. V. Sednev, V. N. Belov, S. W. Hell, Fluorescent dyes with large Stokes shifts for super-

resolution optical microscopy of biological objects: a review. *Methods Appl. Fluoresc.* **3**, 042004 (2015).
35. H. Murakoshi, A. C. E. Shibata, Y. Nakahata, J. Nabekura, A dark green fluorescent protein as an acceptor for measurement of Förster resonance energy transfer. *Sci. Rep.* **5**, 15334 (2015).
36. H. Murakoshi, A. C. E. Shibata, ShadowY: a dark yellow fluorescent protein for FLIM-based FRET measurement. *Sci. Rep.* **7**, 6791 (2017).
37. M. Venkatachalapathy, V. Belapurkar, M. Jose, A. Gautier, D. Nair, Live cell super resolution imaging by radial fluctuations using fluorogen binding tags. *Nanoscale* **11**, 3626–3632 (2019).
38. E. M. Smith, A. Gautier, E. M. Puchner, Single-Molecule Localization Microscopy with the Fluorescence-Activating and Absorption-Shifting Tag (FAST) System. *ACS Chem. Biol.* **14**, 1115–1120 (2019).
39. E. Vicente-García, R. Ramón, R. Lavilla, New Heterocyclic Inputs for the Povarov Multicomponent Reaction. *Synthesis* **2011**, 2237–2246 (2011).
40. Y. Zheng, J. Zhou, D. A. Sayre, H. O. Sintim, Identification of bromophenol thiohydantoin as an inhibitor of DisA, a c-di-AMP synthase, from a 1000 compound library, using the coralyne assay. *Chem. Commun.* **50**, 11234–11237 (2014).
41. J. Ts, *et al.*, Novel 3,5-diaryl pyrazolines and pyrazole as low-density lipoprotein (LDL) oxidation inhibitor. *Bioorg. Med. Chem. Lett.* **14**, 2719–2723 (2004).
42. S. Nakamura, *et al.*, An Arylidene-Thiazolidinedione Derivative, GPU-4, without PPARγ Activation, Reduces Retinal Neovascularization. *Curr. Neurovasc. Res.* **8**, 25–34 (2011).
43. Y. M. Ha, *et al.*, Design and synthesis of 5-(substituted benzylidene)thiazolidine-2,4-dione derivatives as novel tyrosinase inhibitors. *Eur. J. Med. Chem.* **49**, 245–252 (2012).
44. W. A. Cetenko, D. T. Connor, R. J. Sorenson, P. C. Unangst, S. S. Stabler, Known and selected novel arylmethylenyl derivatives of thiazolidinones, imidazolidinones and oxazolidinones useful as antiallergy agents and anti-inflammatory agents, Patent US5208250 (May 4, 1993).
45. V. R. Sirivolu, *et al.*, 5-Arylidenethioxothiazolidinones as Inhibitors of Tyrosyl–DNA Phosphodiesterase I. *J. Med. Chem.* **55**, 8671–8684 (2012).
46. D. G. Gibson, *et al.*, Enzymatic assembly of DNA molecules up to several hundred kilobases. *Nat. Methods* **6**, 343–345 (2009).
47. W. P. Stemmer, Rapid evolution of a protein in vitro by DNA shuffling. *Nature* **370**, 389–391 (1994).
48. A. Crameri, S.-A. Raillard, E. Bermudez, W. P. C. Stemmer, DNA shuffling of a family of genes from diverse species accelerates directed evolution. *Nature* **391**, 288–291 (1998).
49. W. M. Coco, *et al.*, DNA shuffling method for generating highly recombined genes and evolved enzymes. *Nat. Biotechnol.* **19**, 354–359 (2001).
50. R. D. Gietz, R. H. Schiestl, Large-scale high-efficiency yeast transformation using the LiAc/SS carrier DNA/PEG method. *Nat. Protoc.* **2**, 38–41 (2007).
51. A. G. Tebo, F. M. Pimenta, Y. Zhang, A. Gautier, Improved Chemical-Genetic Fluorescent Markers for Live Cell Microscopy. *Biochemistry* **57**, 5648–5653 (2018).
52. L. Dubois, *et al.*, Amino Acids Bearing Aromatic or Heteroaromatic Substituents as a New Class of Ligands for the Lysosomal Sialic Acid Transporter Sialin. *J. Med. Chem.* **63**, 8231–8249 (2020).
53. O. Poirel, *et al.*, LSP5-2157 a new inhibitor of vesicular glutamate transporters. *Neuropharmacology* **164**, 107902 (2020).
54. J. D. Thompson, D. G. Higgins, T. J. Gibson, CLUSTAL W: improving the sensitivity of progressive multiple sequence alignment through sequence weighting, position-specific gap penalties and weight matrix choice. *Nucleic Acids Res.* **22**, 4673–4680 (1994).
55. G. Wu, D. H. Robertson, C. L. Brooks, M. Vieth, Detailed analysis of grid-based molecular docking: A case study of CDOCKER—A CHARMm-based MD docking algorithm. *J. Comput. Chem.* **24**, 1549–1562 (2003).
56. A. Krammer, P. D. Kirchhoff, X. Jiang, C. M. Venkatachalam, M. Waldman, LigScore: a novel scoring function for predicting binding affinities. *J. Mol. Graph. Model.* **23**, 395–407 (2005).
57. J. Huff, The Airyscan detector from ZEISS: confocal imaging with improved signal-to-noise ratio and super-resolution. *Nat. Methods* **12**, i–ii (2015).
58. L. Danglot, *et al.*, Vezatin Is Essential for Dendritic Spine Morphogenesis and Functional Synaptic Maturation. *J. Neurosci.* **32**, 9007–9022 (2012).
59. H. Niwa, K. Yamamura, J. Miyazaki, Efficient selection for high-expression transfectants with a novel eukaryotic vector. *Gene* **108**, 193–199 (1991).
60. A. Edelstein, N. Amodaj, K. Hoover, R. Vale, N. Stuurman, Computer Control of Microscopes Using μManager. *Curr. Protoc. Mol. Biol.* **92**, 14.20.1-14.20.17 (2010).

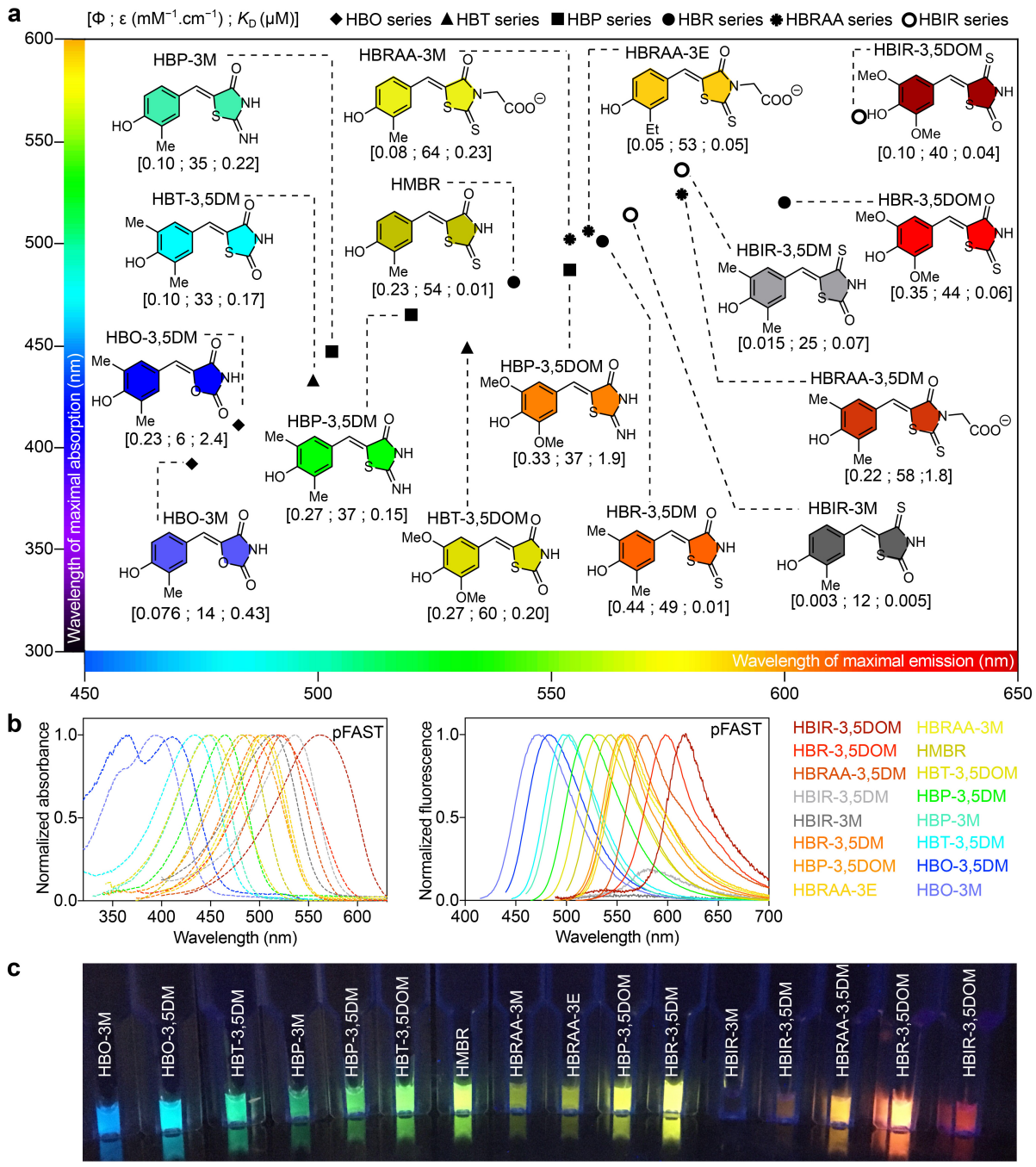

Fig. 1. The engineered protein tag pFAST generates a palette of fluorescent assemblies with the fluorogenic chromophores of the HBO, HBT, HBP, HBR, HBIR and HBRAA series. (a) Structures of the fluorogenic chromophores positioned according to the wavelengths of maximal emission and maximal absorption of their assembly with pFAST. The fluorescence quantum yield (ϕ), molar absorptivity at maximal absorbance (ε) and thermodynamic dissociation constant (K_D) values of their assembly with pFAST are indicated into brackets below the molecules. **(b)** Normalized absorption (left) and fluorescence (right) spectra of the different fluorogenic chromophores bound to pFAST. Spectra were recorded in pH 7.4 PBS at 25°C. Fluorescence spectra were measured by exciting at the maximal absorption wavelength. **(c)** Solutions containing the different pFAST:chromophore assemblies illuminated with 365 nm light.

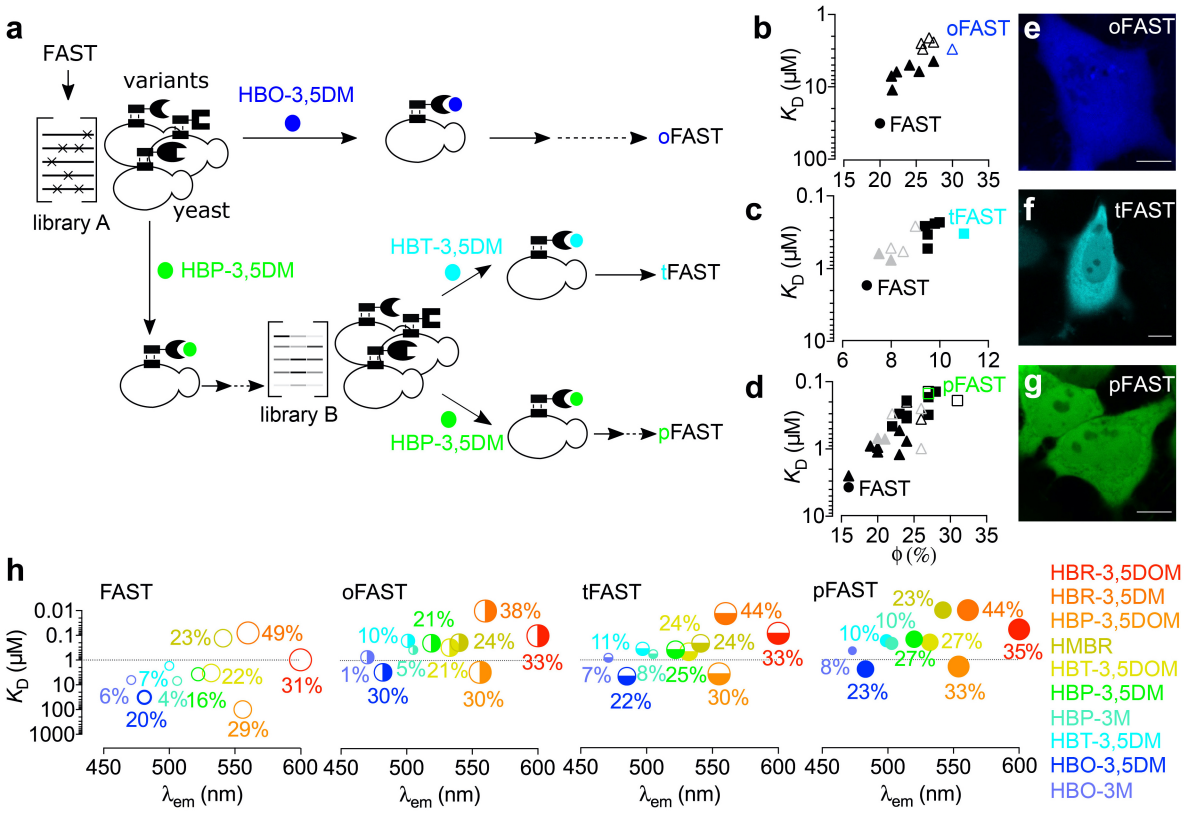

Fig. 2. Engineering of promiscuous FAST variants. (a) Directed evolution allowed the generation of oFAST, tFAST and pFAST. Yeast-displayed libraries of variants of FAST were screened in presence of the indicated fluorogenic chromophore by fluorescence-activating cell sorting (solid arrows). Additional mutations were introduced by rational design (dotted arrows). **(b-d)** K_Ds (thermodynamic dissociation constants) and fluorescent quantum yields (ϕ) of the clones isolated from the selections with (b) HBO-3,5DM, (c) HBT-3,5DM and (d) HBP-3,5DM. Filled triangles are variants from library A ; black squares are variants from library B ; grey triangles are the variants used for the generation of the DNA shuffling library B and unfulfilled triangles and squares are variants generated by rational design. Values are also given for FAST for comparison. **(e-g)** Confocal micrographs of HeLa cells expressing cytoplasmic (e) oFAST labeled with 10 μM HBO-3,5DM, (f) tFAST labeled with 5 μM HBT-3,5DM and (g) pFAST labeled with 5 μM HBP-3,5DM. Scale bars 10 μm. See **Table S12** for imaging settings. **(h)** K_Ds (thermodynamic dissociation constants) and emission wavelength of chromophores of the HBX (X = R, P, T and O) series of fluorogens in presence of FAST variants. Fluorescent quantum yields are given in %.

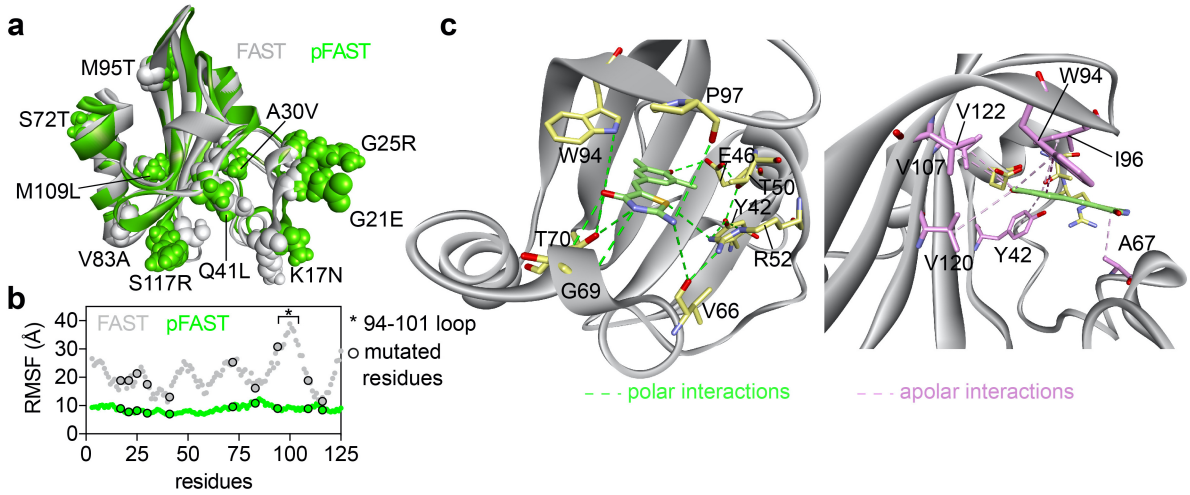

Fig. 3. Structural model of pFAST. **(a)** Structural model of pFAST and FAST generated by homology modeling using the tridimensional crystal structure of the *Halorhodospira halophila* Photoactive Yellow Protein PYP (PDB: 6P4I) (See also **Fig. S6a**). Mutations of pFAST relative to FAST are indicated. **(b)** Root Mean Square Fluctuation (RMSF) of the residues within pFAST and FAST during molecular dynamic simulations. **(c)** Polar and apolar interactions network involved in HBP-3,5DM binding and recognition within pFAST.

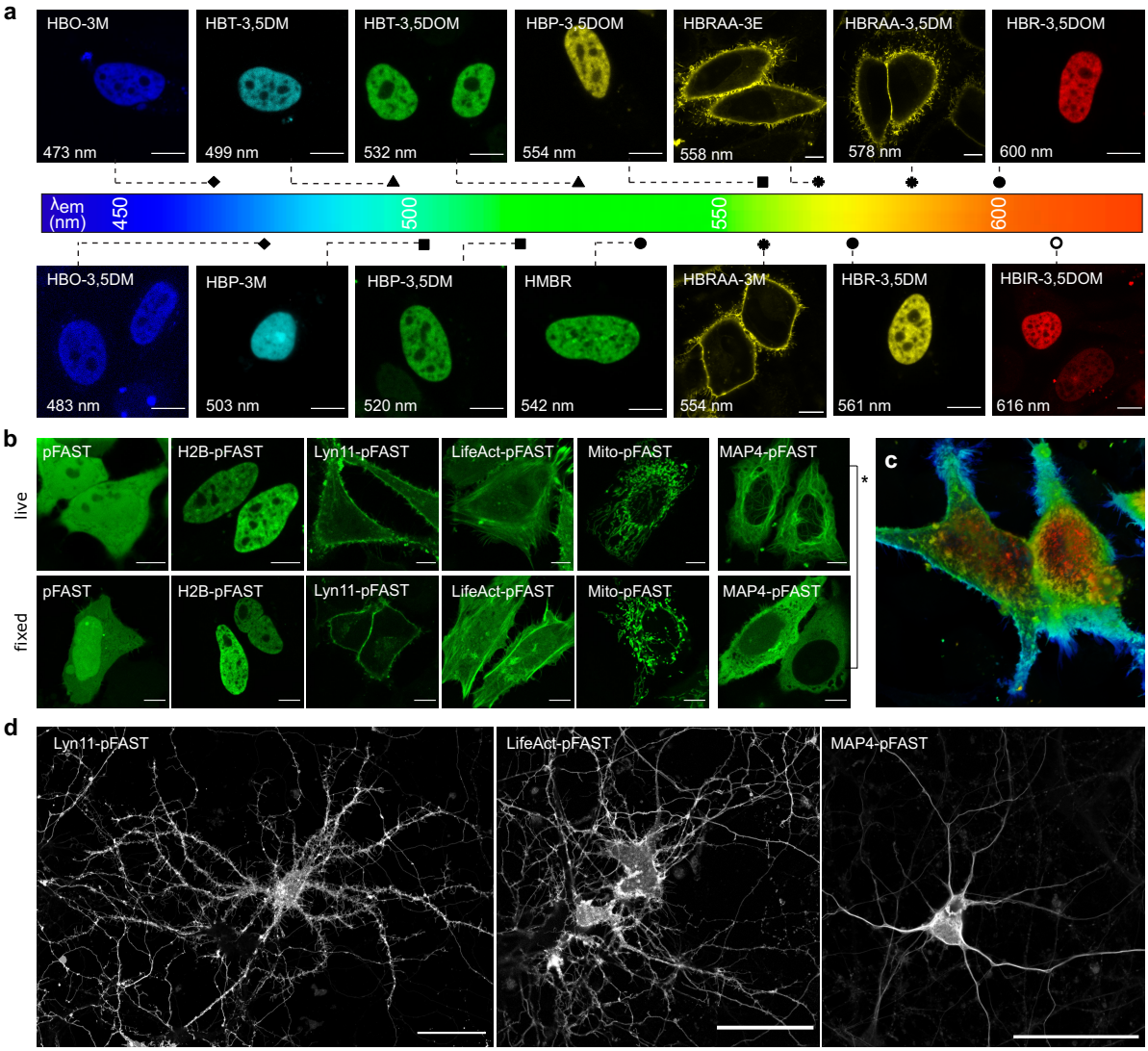

Fig. 4. Selective imaging of pFAST fusions in various cellular localizations in mammalian cells and cultured neurons. (a) Confocal micrographs of HeLa cells expressing pFAST fusions (either with H2B or to a transmembrane domain) in presence of the entire set of fluorogenic chromophores. Scale bars 10 μm. **(b)** Confocal micrographs of live and fixed HeLa cells expressing pFAST fused to: histone H2B, lyn11 (inner membrane-targeting motif), LifeAct (actin binding peptide domain), mito (mitochondrial targeting motif) and to microtubule-associated protein (MAP) 4 and labeled with 5 μM HBP-3,5DM. Note that control experiments showed that the mislocalization of MAP4-pFAST observed in fixed cells (*) was due to MAP4 fixation rather than pFAST (see also **Figure S12**). Scale bars, 10 μm. **(c)** Depth color coded three-dimensional reconstruction (from 81 optical sections) of live HeLa cells expressing lyn11-pFAST fusion and labeled with 5 μM HBR-3,5DOM. **(d)** Confocal micrographs of live dissociated hippocampal neurons expressing pFAST fused to lyn11, LifeAct and MAP4 and labeled with 10 μM HBR-3,5DOM. Scale bars, 50 μm. The Lyn11-pFAST image results from the maximum intensity projection of five optical sections. (**a-d**) See **Table S13** for imaging settings.

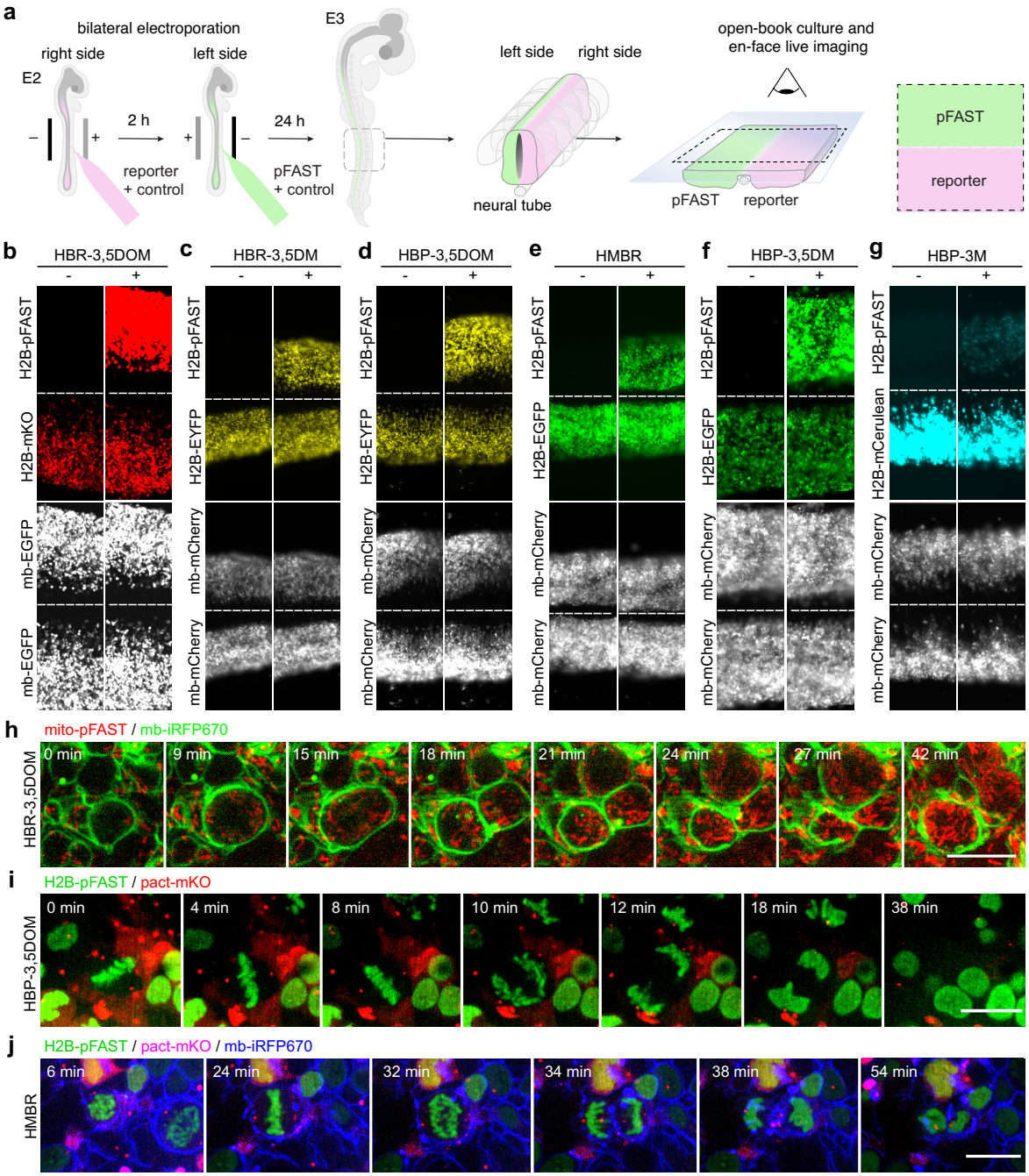

Fig. 5. Selective imaging of pFAST fusions in chicken embryo. (a-g) Plasmids encoding H2B-pFAST and (b) mKO, (c-d) EYFP, (e-f) EGFP and (g) mCerulean fused to H2B were electroporated in each side of the neural tube in ovo at embryonic day 2 (E2, HH stage 13-14). mCherry or EGFP reporters were co-injected with each construct to monitor electroporation efficiency. 24 h later, embryos with homogeneous bilateral reporter expression in the neural tube were dissected and imaged by (b) spinning-disk confocal microscopy or (c-g) widefield fluorescence microscopy before and after addition of the indicated fluorogenic chromophore. **(h-j)** Plasmids encoding (h) mito-pFAST (mitochondrial-targeting motif) and memb-iRFP670 (membrane-targeting motif); (i) H2B-pFAST and pact-mKO (PACT domain of pericentrin) and (j) H2B-pFAST, pact-mKO and mb-iRFP670 were electroporated in the neural tube in ovo, at embryonic day 2 (E2, HH stage 13-14). 24 h later, embryos were dissected, and imaged in presence of (h) 1 μM HBR-3,5DOM , (i) 5 μM HBP-3,5DOM and (j) 1 μM HMBR using a spinning disk confocal microscope. Time-lapse showing cell division presented correct localization of the proteins (see also **Movies S2-S4**). Scale bars, 10 μm. **(a-j)** See **Table S13** for imaging settings.

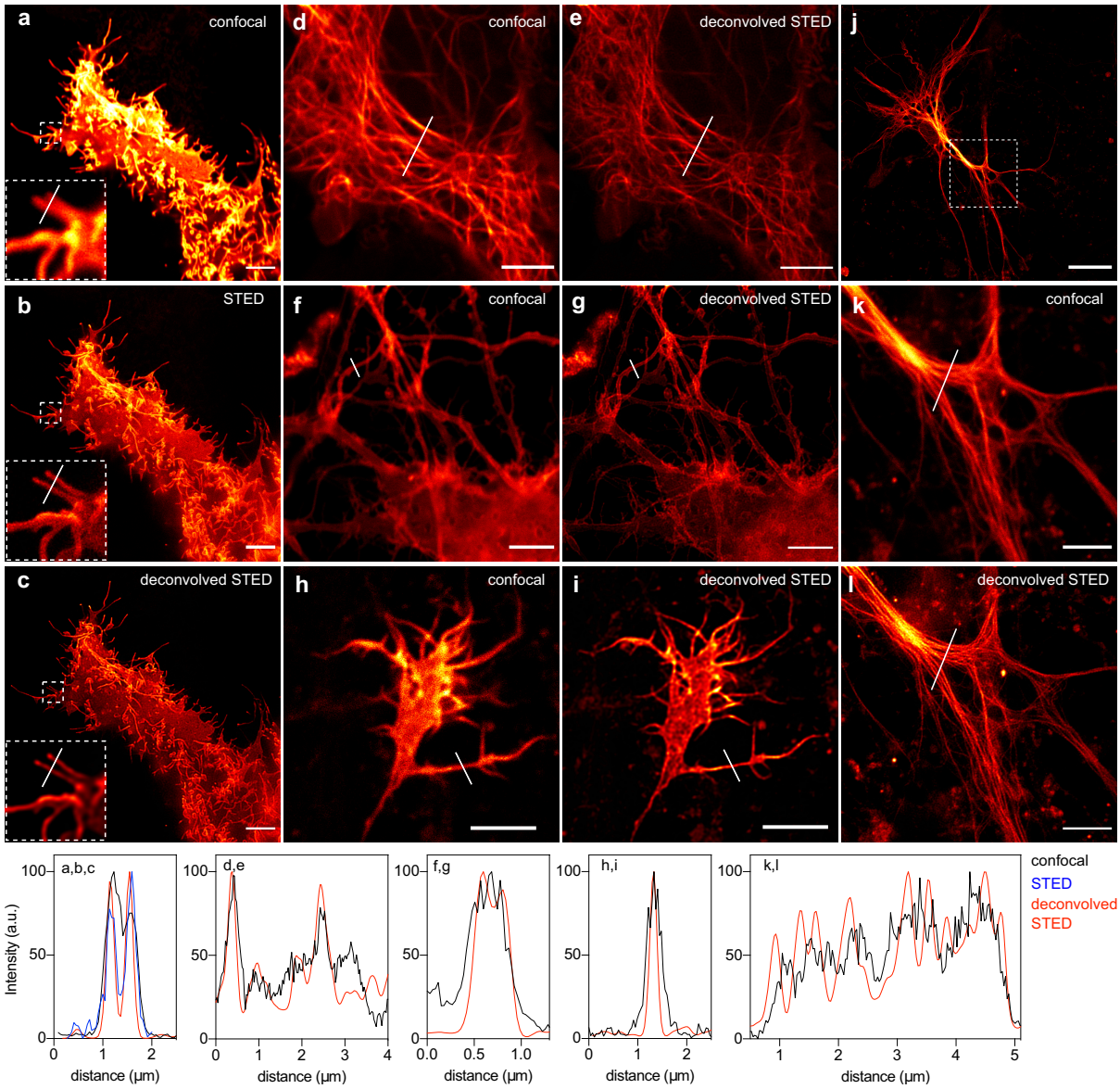

Fig. 6. STED nanoscopy of pFAST-tagged proteins in live mammalian cells, live cultured neurons and live astrocytes. (a-c) Confocal and STED micrographs of live HeLa cells expressing Lyn11-pFAST. **(d,e)** Confocal and STED micrographs of HeLa cells expressing MAP4-pFAST. **(f,g)** Confocal and STED micrographs of live dissociated hippocampal neuron expressing LifeAct-pFAST. **(h,i)** Confocal and STED micrographs of a neurite growth cone expressing LifeAct-pFAST. **(j-l)** Confocal and STED micrographs of a live astrocyte expressing LifeAct-pFAST. Cells were treated with 10 µM of HBR-3,5DOM before imaging. All scale bars are 5 µm, except the one in (i) that is 20 µm. (**a-l)** See **Table S13** for imaging settings. Graphs show gain in resolution.